IEEE Access
Multidisciplinary | Rapid Review | Open Access Journal

Received December 20, 2020, accepted December 29, 2020, date of publication January 5, 2021, date of current version February 3, 2021.

Digital Object Identifier 10.1109/ACCESS.2021.3049236

Dynamic Security and Stability Region Under Different Renewable Energy Permeability in IENGS System

SANIYE MAIHEMUTI[1], WEIQING WANG[1], HAIYUN WANG[1], JIAHUI WU[1], AND XUAN ZHANG[2]

[1]Engineering Research Center of Ministry of Education for Renewable Energy Generation and Grid Connection Technology, Xinjiang University, Urumqi 830047, China

[2]Ship Building Perry Special Gas Company Ltd., Handan 056000, China

Corresponding author: Weiqing Wang (wwq59@sina.com)

This work was supported in part by the Natural Science Foundation of Xinjiang Autonomous Region under Grant 2020D01C068, in part by the National Natural Science Foundation of China under Grant 51667020, and in part by the Natural Science Projects of Scientific Research Program of Universities in Xinjiang Autonomous Region under Grant XJEDU2017I002.

ABSTRACT The integration of renewable energy sources (RESs) remains growing rapidly in recent years. At the same time, security problems after contingencies were attracting great attention, due to deficiencies for the stable operation, even could induce the collapse of integrated energy systems with the deep interconnection of such RESs. To existing issues, the hyper-plane (HP) expression is proved to be an excellent tool for power system situational awareness and stability-constrained operation in practical dynamic security stability regions (PDSSR). In this study, a concept and model were proposed for a high renewable energy penetration of integrated electricity-natural gas system (HRE-IENGS) based on the $N-1$ security guideline. The scheme instruction and system evaluation processes as follows: in order to improve the accuracy of the IENGS system, simulation fitting solutions of PDSSR boundary were presented according to a hybrid algorithm, including dynamic self-adaptive differential evolution algorithm (DSADE), and a least square support vector machine (LSSVM) algorithm. The adopted algorithm approach was applied to rapid approximating of the PDSSR boundary by HP expression in power injection spaces. Simultaneously, different renewable energy permeabilities (DREPs) were set from 5 to 50 %, and active power injections of DREPs under short circuit fault on IEEE 118 bus system simulated by using DIgSLENT/power factory software. As the consequence, this mentioned method effectively described the security stability boundary of HRE-IENGS, and realized the three-dimensional visualization space of DREPs-PDSSR. In addition, the behavior of operation points and PDSSR under DREPs were carefully investigated, and unstable runs were accurately exposed. Through the PDSSR, the state analysis could be conducted rapidly on several parameters, including security and stability assessment with various energy supply capabilities. Meanwhile, these indexes were calculated offline and applied on-line. The results of this study verified the accuracy and effectiveness of the proposed modeling for the considered system, and thus could provide technical support for the stability of the HRE-IENGS system.

INDEX TERMS Integrated energy system, renewable energy, dynamic security stability region, DSADE algorithm, LSSVM.

I. INTRODUCTION

High penetration of renewable energy sources (RESs) such as the non-rotational nature of solar photovoltaic (PV) generators and the variable speed wind turbine (WT) generators affects the interdependence between electricity networks and natural gas networks (NGNs) in many aspects [1]. steady increase of variable demand for electricity due to rapid global economic growth, fossil fuel depletion, and, more importantly, environmental concerns associated with fossil fuel-based energy systems, make the transition towards RESs an inevitable choice. However, compared to the conventional power system, the RESs have different technical characteristics. Therefore, connecting high levels of intermittent

The associate editor coordinating the review of this manuscript and approving it for publication was Siqi Bu.

This work is licensed under a Creative Commons Attribution 4.0 License. For more information, see https://creativecommons.org/licenses/by/4.0/

RESs creates additional challenges to maintain the stability of electrical transmission systems, either during normal operation or in the event of abnormal disturbances. For example, the gas-fired generator has been widely adopted to fulfill the fast response, requirement of electricity networks due to the intermittency of RESs [2]. Moreover, the power to gas technology and combined cooling, heating, and power (CCHP) technology can convert, store, transfer, and consume the surplus energy in different states [3]. The electricity-gas interdependence facilitates the flexibility of the electricity network with high penetration of RESs. Therefore, high renewable energy penetration of integrated electricity natural gas system (HRE-IENGS) represents an ideal low-carbon sustainable energy system.

The accelerating interdependence between electricity networks and NGNs can boost the RE integration and increase the concern about the security and stability of HRE-IENGS [4]. Compared to the single energy system, the integrated system has new operation characteristics and security constraints, and brings the risk of cascading failures between systems [5]. Therefore, research on the security and stability challenges of the HRE-IENGS system with high RESs is highly beneficial. Security and stability are two of the most crucial topics for HRE-IENGS operation. In general, sources of uncertainty in HRE-IENGS system include renewable generation fluctuation (such as wind power and PV power) [6], load variation [7], $N-1$ contingencies [8], and malicious attacks [9]. However, eco-friendly renewables introduce operational uncertainties that would jeopardize the HRE-IENGS system. Till date, several methods have been proposed to address the security challenges of the IES, such as fluctuation sensitivity [10], integrated dynamic simulation [11], unified steady-state power flow [12], optimal energy flow [13], and so on. Literature studies [14] modeled and assessed the reliability and interaction between the power systems and natural gas systems. Reference [15] carried out a static safety analysis on the impact of different disturbances on the electric thermal coupling system in the expected accident concentration. A literature study [16] proposed a joint optimization model of a thermoelectric integrated energy system considering static safety factors. A novel formulation of security-constrained optimal power and gas flow was also presented [17], where $N-1$ contingency did not lead to violations by adjusting state variables in advance. Furthermore, a security-constrained bi-level economic dispatch model for integrated electricity and natural gas systems [2]. Reference [18] proposed a security-constrained co-planning of power lines and energy storage, where $N-1$ emergency overflow was considered. The above-mentioned researches mainly utilized the optimal power flow method to ensure system security. These studies did not carry out a comprehensive overall measurement of the integrated multi-energy system, and could not obtain the maximum operating boundary and adjustable margin of the system.

Therefore, researchers proposed the concept of ''security stability region, SSR''. Among these, SSR is considered as a powerful tool, which was first introduced in the electricity network and defined as a set of operation points to satisfy the power flow equation and security and stability constraints. It describes the largest region of the entire system that can operate safely, which has been widely used in power systems. Meaningful information for the operators such as the security margin and optimal control decision has been provided according to the relative relation between the operating point and security boundary. Moreover, for the specific security and stability issue, the static security stability region (SSSR), transient security stability region (TSSR) and dynamic security stability region (DSSR) are deduced. At present, the research on SSSR has become relatively mature in modern power systems than the latter two. The research on ''SSSR'' proposed in the literature study [19] could improve the shortcomings of static security analysis of multi-energy systems to a certain extent. An algorithm to construct inner approximations of static security was developed [20]. Furthermore, the maximal static security region was also proposed [21]. A new stochastic optimal power flow considering the static security constraints was presented in a literature report [22]. According to the literature [30], the distance to the boundaries of the security region was used for the SSSR construction. Further, the evaluation of the system SSSR for multiple contingencies was performed [24] by employing a multiway decision tree. The security region of NGNs in IES was studied, considering the influence of the electricity network and NGNs [25]. According to the literature [26], a direct method for the practical dynamic security region of the electric power system was presented under different critical power injections. Furthermore, security assessment and preventive control based on the dynamic security region were proposed in the power system [27], wherein quadratic and linear approximations were used for boundary calculation. However, for the HRE-IENGS, the existing dynamic security region research is still relatively shallow, and the dynamic security region considering the $N-1$ security guideline has not been satisfied.

In this study, the DSSR of HRE-IENGS system was mainly investigated. In particular, given the system components' parameters and network topology, the DSSR that satisfies the transient angle stability in the nodal injection space has the following properties: (1) the DSSR is unique and does not vary with the operating states. (2) for practical engineering application, the DSSR boundary can be approximately described by one or several hyper-planes (HPs). Accordingly, the mathematical description of the security constraint is a linear combination inequality of power injection variables, which has great advantages in security monitoring, probabilistic security assessment, and a series of optimization problems. In recent years, with the integration of a great amount of uncertain RESs [28]–[30], the DSSR with the hyper-plane expression, known as practical DSSR (PDSSR), undoubtedly becomes a powerful tool to cope up with various optimization problems accounting for the transient angle stability and nodal injection uncertainty. Moreover, the HP coefficients calculated off-line, stored in the database and

applied on-line. Therefore, how to obtain the HP expression of the PDSSR boundary quickly and accurately is the critical step.

At present, the calculation methods for the PDSSR boundary are mainly classified into fitting [31] and analytical methods [32], as well as many improved methods based on them [33]–[38]. The analytical method generally derives the analytical expression of the PDSSR boundary by using the mapping relationship between the nodal injection power and the system transient stability states, which is computationally efficient, but not accurate enough. In contrast, the fitting method includes two steps: the first step involves the searching of sufficient critical points (the one where the normal initial operation point extending outwards continuously meets the SR boundary for the very first time), through massive simulation; the second step involves the fitting of the analytical expression of the PDSSR boundary based on the critical points. The fitting method has high accuracy; however, the computational burden is very heavy. As a result, the fitting method is usually employed as the reference method. It can be found that the key to obtaining PDSSR boundary is locating enough critical points as quickly as possible and then fitting effectively, in particular, the challenging part is locating critical points quickly from a large number of operating points in the high-dimension nodal injection space. Therefore, we also developed a general meta-heuristic algorithm to form the PDSSR in HRE-IENGS system. In recent years, the differential evolution (DE) algorithm and least square support vector machine (LSSVM) method have shown much faster speed, higher accuracy, and widespread applicability, which can be supplementary to the model-based method. This study introduced a DSADE-LSSVM algorithm for identifying key generators with high efficiency. The major contributions of this study are summarized as follows.

- Herein, considering the strong intermittency of RESs, an HRE-IENGS system is composed of an external power grid, RESs and NGNs to meet the diversified energy and social demands of consumers. In order to improve the reliability of the proposed HRE-IENGS system, the dynamic security and stability were studied and a novel concept and mathematical expressions of the proposed system and its security and stability region were provided.
- In order to find out the critical security stability operation region of HRE-IENGS system more quickly and accurately, this study further improved and combined the advantages of DSADE algorithm and LSSVM algorithm. Further, a novel hybrid DSADE-LSSVM algorithm was proposed to search the maximum dynamic security and stability operation region under the fault of $N-1$.
- According to the IENGS system with different permeability of RESs, the optimal HP coefficient was obtained under the constraint of DSADE-LSSVM HP, and the PDSSR of the system was fitted and analyzed.

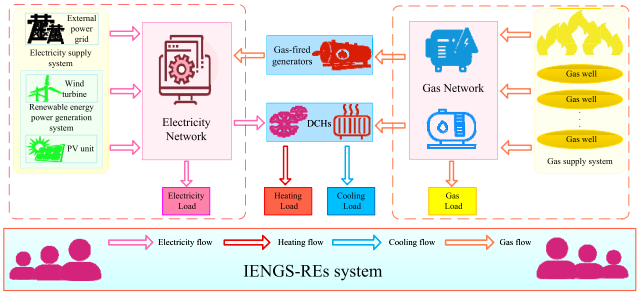

FIGURE 1. The framework of the HRE-IENGS.

The remaining part of this paper is organized as follows: Section II and Section III elaborate on the HRE-IENGS model and solution, which are the concept and definition of the electricity supply network, NGNs, and energy hub in HRE-IENGS. Section IV provides a detailed description of the DSSR model, security, and stability constraints. In section V, a novel hybrid DSADE-LSSVM algorithm based on DSADE and LSSVM is proposed. Section VI presents the simulation of the PDSSR in the New England 118 bus system with different permeability of RESs and presents the security stability analysis for the simulation results. Section VII presents the conclusions and outlooks.

II. STEADY STATE MODEL OF HRE-IENGS

A. FRAMEWORK OF THE HRE-IENGS

The framework of HRE-IENGS system considered in this study is given in Fig. 1. The HRE-IENGS consists of NGNs, an electricity network, and distributed cooling and heating stations (DCHs). In particular, the electricity network and NGNs are connected through a gas-fired generator. Furthermore, electricity supply systems are connected to the electricity network for embedding high penetration of renewable energies to supply electricity load. The renewable energy power generation system consists of WT and PV. The gas part includes a gas supply system and gas network to supply gas load. Through a series of energy conversion, DCHs supply cooling and heating loads. HRE-IENGS realizes the conversion of different energy forms and complements each other's advantages interconnected via energy networks, respectively, and improves the stability and reliability of energy use.

B. STEADY STATE MODEL OF ELECTRICITY NETWORK

The power flow calculation (PFC) of the power system is consistent with the AC-PFC of the traditional system. The node power deviation equation can be written as follows:

$$\Delta P_i = P_i^{\mathrm{GG}} + P_i^{\mathrm{DCH}} + P_i^{\mathrm{EG}} - P_i^{\mathrm{ED}} - P_i^{\mathrm{GC}} - P_i^{\mathrm{HP}} - P_i^{\mathrm{EB}} - V_i \sum_{j\in i} V_j \left(G_{ij}\cos\theta_{ij} + B_{ij}\sin\theta_{ij}\right) \quad (1)$$

$$\Delta Q_i = Q_i^{\mathrm{EG}} + Q_i^{\mathrm{SH}} - Q_i^{\mathrm{ED}} - V_i \sum_{j\in i} V_j \left(G_{ij}\cos\theta_{ij} - B_{ij}\sin\theta_{ij}\right) \quad (2)$$

where P_i and Q_i are the active and reactive power injected by node i, respectively; U_i and U_j are the voltage of node i and j, respectively; G_{ij} and B_{ij} are the conductance and admittance of node admittance matrix, respectively; and θ_{ij} is the voltage phase angle difference between node i and node j. P_i^{EG}, Q_i^{EG} inject power into the generator; P_i^{ED}, Q_i^{ED} corresponds to the power consumed by power load at bus i; P_i^{GG}, P_i^{DCH} is the active power injected into bus i by a gas generator and DCHs unit, respectively; P_i^{GC}, P_i^{HP}, P_i^{EB} are the active power consumed by the electric compressor, circulating pump of the heat supply network and electric boiler respectively; and Q_i^{SH} is the reactive power injected by the reactive power compensator.

C. STEADY STATE MODEL OF NGNs

The natural gas system is mainly composed of a pipeline, pressure station, connection node, and other basic components. The pipeline transports and distributes the natural gas injected into the network to the load side, and the pressure station can increase the pressure of the pipeline to supplement the pressure loss in the process of energy transmission. Assuming that there is no height difference between the two ends of the natural gas pipeline and the gas flow is isothermal [39], the nodal flow deviation equation is represented as follows:

$$\Delta f_i = f_i^{\mathrm{GS}} - f_i^{\mathrm{GD}} - f_i^{\mathrm{GG}} - f_i^{\mathrm{DCH}} - f_i^{\mathrm{GB}} - f_i^{\mathrm{GC}} - \sum_{j\in i} C_{ij}^{\mathrm{Gp}} \mathrm{sign}_{ij} \sqrt{\mathrm{sign}_{ij}\left(\Pi_i^2 - \Pi_j^2\right)} \quad (3)$$

where f_i^{GS} and f_i^{GD} are the gas injection and load flow at node i, respectively; f_i^{GG}, f_i^{DCH}, f_i^{GB} are the natural gas flow consumed by gas generator, DCHs unit, and gas boiler, respectively; C_{ij}^{Gp} is the constant of the natural gas pipeline; $sign_{ij}$ is the flow direction of natural gas in the pipeline. When the pressure of node i is greater than that of node j, $sign_{ij}$ is $+1$, otherwise it is -1.

D. STEADY STATE MODEL OF DCH SYSTEM

The energy transfer of the thermal system is mainly in the form of hot water or steam, from the heat source to consumers. Therefore, the thermal network not only satisfies Kirchhoff's law, but also includes the temperature solution model:

$$T_{\mathrm{end}} = (T_{\mathrm{end}} - T_a)\, \mathrm{e}^{\frac{-\lambda l}{C_p \dot{m}}} + T_a \quad (4)$$

$$\left(\sum \dot{m}_{\mathrm{out}}\right) T_{\mathrm{out}} = \left(\sum \dot{m}_{\mathrm{in}} T_{\mathrm{in}}\right) \quad (5)$$

where T_{end} and T_{start} are the temperatures at the end and head of the pipeline respectively; T_a is the ambient temperature; λ is the thermal conductivity coefficient of the unit pipeline; and l is the length of the pipeline. Equation (5) is used to calculate the temperature of mass flow leaving the node after mixing in multiple pipes. In generally, the heating temperature T^s at the heat source and the outlet temperature T^r of each load before mixing are known. The temperature of unknown nodes is calculated by using equation (4) and (5). The deviation equation of thermodynamic system is as follows:

$$\Delta\phi_i = \phi_i^{\mathrm{EB}} + \phi_i^{\mathrm{GB}} + \phi_i^{\mathrm{DCH}} - \phi_i^{\mathrm{HD}} - \sum_{j\in i} C_p \dot{m}_{ij}\left(T_i^s - T_i^r\right) \quad (6)$$

$$\Delta\sigma_i = \boldsymbol{B}_h K_h \dot{m}\,|\dot{m}| \quad (7)$$

$$\Delta T_i^s = \boldsymbol{C}_s T_i^s - \boldsymbol{B}_s \quad (8)$$

$$\Delta T_i^r = \boldsymbol{C}_r T_i^r - \boldsymbol{B}_r \quad (9)$$

where ϕ_i^{EB}, ϕ_i^{GB}, and ϕ_i^{DCH} are electric boilers, gas-fired boilers, and DCHs units providing heat power for heat supply network, respectively; ϕ_i^{HD} is heat power required by node load; C_p is the -specific heat capacity of water; $\dot{m}_{ij}$ is mass flow of pipeline from node i to node j. The matrix $\boldsymbol{B}_h$ is the loop network correlation matrix [47]; K_h is the resistance coefficient of the pipeline; $\boldsymbol{C}_s$, $\boldsymbol{C}_r$ are the temperature coefficient matrix; and $\boldsymbol{B}_s$, $\boldsymbol{B}_r$ are the column vectors including temperature and mass flow.

E. MODEL ESTABLISHMENT OF COUPLING EQUIPMENT

The coupling equipment realizes the function of energy interaction and distribution. In order to fully consider the energy conversion relationship among various energy carriers, this paper mainly introduces the following coupling equipment model: gas-fired boilers, DCHs units, and gas-fired generators, as loads of NGNs, provide energy for heat supply network and power grid, respectively. The model [48], [49] is as follows:

$$f_i^{\mathrm{B}} = 3.412 \frac{\phi_i^{\mathrm{B}}}{\eta_i^{\mathrm{B}} \mathrm{GHV}} \quad (10)$$

$$f_i^{\mathrm{DCH}} = 3.412 \frac{P_i^{\mathrm{DCH}} + \phi_i^{\mathrm{DCH}}}{\eta_i^{\mathrm{DCH}} \mathrm{GHV}} \quad (11)$$

$$f_i^{\mathrm{GG}} = \frac{a_i^{\mathrm{GG}}\left(P_i^{\mathrm{GG}}\right)^2 + b_i^{\mathrm{GG}} P_i^{\mathrm{GG}} + c_i^{\mathrm{GG}}}{\mathrm{GHV}} \quad (12)$$

where η_i^{B} and η_i^{DCH} are conversion efficiency of the gas-fired boiler and DCHs unit, respectively; a_i^{GG}, b_i^{GG}, c_i^{GG} denote the operation coefficient of the i^{th} gas-fired generator; GHV is the calorific value of natural gas, BTU / m^3; 3.412 is the unit conversion coefficient to convert W to BTU / h.

Electric compressor, circulating pump, and electric boiler provides energy for NGNs and heat supply network as power system load. The model is as follows:

$$P_i^{\mathrm{GC}} = \frac{746 \times 10^{-6}}{3600} E_i^{\mathrm{GC}} \quad (13)$$

$$P_i^{\mathrm{HP}} = \frac{\dot{m}_i^{\mathrm{HP}} g H_p}{10^6 \eta_{\mathrm{HP}}} \quad (14)$$

$$P_b = \frac{\phi_b}{\eta_b} \quad (15)$$

where E_i^{GG} is the required energy of the compressor; when this part of the energy is provided by the power grid, the consumed electric power is P_i^{GG}; η_{HP}, η_b are the circulating pump

efficiency and the heat production efficiency of the electric boiler, respectively; and H_p is the pump head.

III. THE STEADY STATE SOLUTION OF HRE-IENGS

At present, the multi-energy power flow is usually employed to analyze the steady-state solution of the HRE-IENGS integrated energy system which is composed of an electricity network, NGNs and high penetration of RESs with a certain radiation range as shown Fig. 2. The basic idea of this method is similar to the steady-state power flow analysis of the power system. By constructing the given operating conditions and network structure, the operating status of the current HRE-IENGS system was analyzed. The energy flow analysis of the HRE-IENGS system is of great significance to system planning, maintenance, and accident prediction. The hybrid power flow analysis of the integrated energy system is the basis of stability calculation and fault analysis of HRE-IENGS system.

Although the physical models of the electricity networks, NGNs, and DCHs systems are different, the network structure satisfies the energy conservation and Kirchhoff law. Many scholars have studied the steady-state analysis model of energy flow in the integrated energy system. The study of the hybrid power flow analysis method indicates that in order to build the grid structure of natural gas, heat, and other grid structures with the electricity network as a unified whole for the solution, high-dimensional non-linear equations are constructed by combining the mathematical model of grid structure and equipment of non-power system with the power flow equation through energy conservation and Kirchhoff law. The power flow model is represented as follows:

$$\begin{cases} 0 = F\left(x_{\mathrm{e}}, x_{\mathrm{g}}, x_{\mathrm{h}}, x_{\mathrm{EH}}\right) \\ 0 = G\left(x_{\mathrm{e}}, x_{\mathrm{g}}, x_{\mathrm{h}}, x_{\mathrm{EH}}\right) \\ 0 = H\left(x_{\mathrm{e}}, x_{\mathrm{g}}, x_{\mathrm{h}}, x_{\mathrm{EH}}\right) \\ 0 = EH\left(x_{\mathrm{e}}, x_{\mathrm{g}}, x_{\mathrm{h}}, x_{\mathrm{EH}}\right) \end{cases} \tag{16}$$

where F, G, H and EH represent the algebraic equations of the electricity network, NGNs, DCHs system, and energy hub, respectively; x_{e} represents variables related to the electricity network, such as node voltage and node power; x_{g} refers to variables related to NGNs, such as pipeline flow, pipe network node pressure, etc.; x_{h} refers to variables related to DCHs system, such as the inlet/return water temperature, heating/cooling power, etc; and x_{EH} represents the variables related to the energy hub, usually the energy distribution coefficient.

Newton Raphson is the basic method to solve the hybrid power flow model of HRE-IENGS system. The Jacobian matrix of Newton Raphson can reflect the coupling relationship between different energy flows as follows:

$$\begin{cases} x^{(k+1)} = x^{(k)} - \Delta x^{(k)} \\ \Delta x^{(k+1)} = \left(J^{(k)}\right)^{-1} \Delta F^{(k)} \\ \Delta x^{(k+1)} = \left(J^{(k)}\right)^{-1} \Delta G^{(k)} \end{cases} \tag{17}$$

$$J = \begin{bmatrix} J_{\mathrm{ee}} & J_{\mathrm{eh}} & J_{\mathrm{eg}} \\ J_{\mathrm{he}} & J_{\mathrm{hh}} & J_{\mathrm{hg}} \\ J_{\mathrm{ge}} & J_{\mathrm{gh}} & J_{\mathrm{gg}} \end{bmatrix} = \begin{bmatrix} \dfrac{\partial F}{\partial x_{\mathrm{e}}} & \dfrac{\partial G}{\partial x_{\mathrm{e}}} & \dfrac{\partial H}{\partial x_{\mathrm{e}}} \\ \dfrac{\partial F}{\partial x_{\mathrm{h}}} & \dfrac{\partial G}{\partial x_{\mathrm{h}}} & \dfrac{\partial H}{\partial x_{\mathrm{h}}} \\ \dfrac{\partial F}{\partial x_{\mathrm{g}}} & \dfrac{\partial G}{\partial x_{\mathrm{g}}} & \dfrac{\partial H}{\partial x_{\mathrm{g}}} \end{bmatrix} \tag{18}$$

where the diagonal elements J_{ee}, J_{hh} and J_{gg} of Jacobian matrix, respectively, represent the power flow and vector state of power subsystem, heat pipe network and NGNs. Each off-diagonal matrix represents the coupling relationship between two energy sources. If there is a coupling relationship between two energy sources, the corresponding off-diagonal elements are not zero; and if there is no coupling relationship, then it is zero. Owing to the difference of system coupling mode and equivalent modeling method, the solution of hybrid power flow is also different.

The security region of HRE-IENGS system is a set of node injections of all operating points that satisfy the MEPF equation and operation safety constraints. It includes three groups of equations, including power flow and constraint of the electricity network, energy flow and constraint of NGNs, and constraint conditions of an energy hub, as shown in (19) - (21):

$$\begin{cases} f_{\mathrm{e}}\left(P, Q, V, \theta\right) = 0 \\ \Delta L_{\mathrm{e}} = L_{\mathrm{e}} - P_{\mathrm{e}} \\ 0 \le P_{\mathrm{e}} \le L_{\mathrm{e}} \\ P_{\min} \le P \le P_{\max} \\ Q_{\min} \le Q \le Q_{\max} \\ V_{\min} \le V \le V_{\max} \\ \theta_{\min} \le \theta \le \theta_{\max} \end{cases} \tag{19}$$

where L_{e} is the node load of the power system; P_{e} is the node power flow of the power system; P, Q, V, and θ are the active power flow, reactive power flow, voltage, and phase angle of the power system respectively, and the upper and lower limits of their values are represented in the equation; and f_{e} is the node power equation of the relationship between the injected power and the node voltage.

$$\begin{cases} \boldsymbol{A}F_{mn} + S - L - \boldsymbol{G}F_c = 0 & \text{(a)} \\ \begin{cases} f_{\mathrm{g}}\left(F_{mn}, H_c, p\right) = 0 \\ \Delta L_g = L_g - P_g \\ 0 \le P_g \le L_g \\ (F_{mn})_{\min} \le F_{mn} \le (F_{mn})_{\max} \\ (H_c)_{\min} \le H_c \le (H_c)_{\max} \\ p_{\min} \le p \le p_{\max} \end{cases} & \text{(b)} \end{cases} \tag{20}$$

where 20 (a), $\boldsymbol{A}$ is the topological matrix of the system; S is the output of the gas network node; L is the node load demand; $\boldsymbol{G}$ is the correlation matrix between the compressor and the node, and F_{c} is the gas consumption of the compressor. In 20 (b), L_{g} is the node load of NGNs; P_{g} is the nodal power flow of natural gas system; F_{mn}, H_{c}, and p denote branch flow of NGNs, compressor power, and node air pressure,

respectively, and the upper and lower limits of their values are expressed in the equation; and f_g is the power flow equation of NGNs.

$$\begin{cases} L = CP & \text{(a)} \\ \begin{cases} \Delta L = L_0 - L \\ P_{\min} \le P \le P_{\max} \\ 0 \le L \le L_0 \end{cases} & \text{(b)} \end{cases} \tag{21}$$

where $P_{\min}$ and $P_{\max}$ are the lower and upper limits of active power, and L_0 is the initial input electric/gas/heat load of the energy hub.

The dynamic response time of the power grid is usually from seconds to minutes, and the dynamic response time of gas and heating networks is usually from minutes to hours. If the time scale of the power network with the fastest dynamic change is used as the benchmark, the dynamic state estimation of the gas network and the heating network will generate a lot of useless calculations, and the calculation efficiency is low. Similarly, if the time scale of the gas grid or the heating grid is used as the standard for dynamic state estimation, the dynamics of the grid will be difficult to reflect, resulting in reduced calculation accuracy. The basic mathematical model of mixed time scale operation optimization is:

$$\begin{cases} \min f\left(x_{\mathrm{e}}^{t_{\mathrm{e}}}, x_{\mathrm{g}}^{t_{\mathrm{g}}}, x_{\mathrm{h}}^{t_{\mathrm{h}}}\right) \\ s.t.\ g_{\mathrm{e}}\left(x_{\mathrm{e}}^{t_{\mathrm{e}}}\right) \le 0, \quad g_{\mathrm{g}}\left(x_{\mathrm{g}}^{t_{\mathrm{g}}}\right) \le 0,\ g_{\mathrm{g}}\left(x_{\mathrm{h}}^{t_{\mathrm{h}}}\right) \le 0 \\ \quad x_{\mathrm{e,g}}^{t_{\mathrm{e}}} = x_{\mathrm{g,e}}^{t_{\mathrm{g}}} \quad \forall t_{\mathrm{g}} \in T_{\mathrm{g}}\left(t_{\mathrm{g}}\right) \\ \quad x_{\mathrm{e,h}}^{t_{\mathrm{e}}} = x_{\mathrm{h,e}}^{t_{\mathrm{h}}} \quad \forall t_{\mathrm{h}} \in T_{\mathrm{h}}\left(t_{\mathrm{e}}\right) \\ \quad x_{\mathrm{g,h}}^{t_{\mathrm{g}}} = x_{\mathrm{h,g}}^{t_{\mathrm{h}}} \quad \forall t_{\mathrm{g}} \in T_{\mathrm{g}}\left(t_{\mathrm{e}}\right),\ t_{\mathrm{h}} \in T_{\mathrm{h}}\left(t_{\mathrm{e}}\right) \\ \quad x_{\mathrm{g,e}}^{t_{\mathrm{g}}} = x_{\mathrm{g,e}}^{t_{\mathrm{g}}'} \quad \forall t_{\mathrm{g}}, t_{\mathrm{g}}' \in T_{\mathrm{g,e}}\left(t_{\mathrm{g,e}}\right) \\ \quad x_{\mathrm{h,e}}^{t_{\mathrm{h}}} = x_{\mathrm{h,e}}^{t_{\mathrm{h}}'} \quad \forall t_{\mathrm{h}}, t_{\mathrm{h}}' \in T_{\mathrm{h,e}}\left(t_{\mathrm{h,e}}\right) \end{cases} \tag{22}$$

Among them t_{e}, t_{g} and t_{h} are time indexes of power, gas and heating subsystems respectively, where t_{e} is consistent with the dispatching time interval of the power system; x_{e}, x_{g}, x_{h} are decision variables of each subsystem; $f(\cdot)$ is the objective function of operation optimization; $g_{\mathrm{e}}(\cdot) \le 0$, $g_{\mathrm{g}}(\cdot) \le 0$ and $g_{\mathrm{h}}(\cdot) \le 0$ are their own operation constraints; $x_{\mathrm{e,g}}$, $x_{\mathrm{e,g}}$ are power system part and gas system part in coupling variables of the power system and gas system; where $x_{\mathrm{e,h}}$, $x_{\mathrm{h,e}}$ are power system part and heating system part in coupling variables of the power system and heating system respectively; $x_{\mathrm{g,h}}$, $x_{\mathrm{h,g}}$ are the gas system part and heating system part in the coupling variables of the gas system and heating system respectively; $T_{\mathrm{g}}(t_{\mathrm{e}})$ and $T_{\mathrm{h}}(t_{\mathrm{e}})$ are the time index set of gas and heating system corresponding to the t_{e} dispatching interval respectively; $x_{\mathrm{g,e}}$, $x_{\mathrm{h,e}}$ are the state variables corresponding to the schedulable equipment in the gas system and heat supply system respectively; $t_{\mathrm{g,c}}$, $t_{\mathrm{h,c}}$ are the cycle index of the dispatching instructions of the gas system and the heating system respectively; $T_{\mathrm{g,c}}(t_{\mathrm{g,c}})$ is the gas system time index set corresponding to the $t_{\mathrm{g,c}}$ scheduling instruction cycle; $T_{\mathrm{h,c}}(t_{\mathrm{h,c}})$ is the time index set of the heating system corresponding to the $t_{\mathrm{h,c}}$ scheduling instruction cycles. Group 4-6 constraints in equation (22) are state constraints generated by coupling relationship between subsystems; The 7, 8th group of constraints is gas system and heating system state constraints respectively, indicating that the state variables corresponding to the operational equipment in the gas system/heating system should be consistent in the same operation instruction cycle.

IV. MATHEMATICAL MODEL OF HRE-IENGS DYNAMIC SECURITY STABILITY REGION

A. SECURITY CONSTRAINTS AND SECURITY DOMAINS OF POWER SYSTEM

The constraints of safe and stable operation of power system include voltage amplitude constraint, line current constraint, active power generation constraint, and security constraint set. If it is assumed that there is $n+1$ node in the power system, 0 is the slack node, $1 \sim n_0$ is the generator node, and $n_0 + 1 \sim n$ is the load node.

1) VOLTAGE AMPLITUDE CONSTRAINT IN POWER SYSTEM

The nodes in the power system are divided into the following two types: One is the node of the generator, and G is the set of generator nodes. The other is the load node, which is represented by L. The voltage constraint set is defined as follows:

$$\mathfrak{R}_{Vr} := \mathfrak{R}_{V(L)r} \times \mathfrak{R}_{V(G)r} \tag{23}$$

Among them:

$$\mathfrak{R}_{V(L)} := \left\{ V_L \left| V_L^{\min} \le V_L \le V_L^{\max} \right| V_L \in \boldsymbol{R}^{(n-n_0)} \right\} \tag{24}$$

$$\mathfrak{R}_{V(G)} := \left\{ V_G \left| V_G^{\min} \le V_G \le V_G^{\max} \right| V_G \in \boldsymbol{R}^{n_0} \right\} \tag{25}$$

where r is the set of constraints in incremental form; V_G is the voltage of the generator; V_L is the voltage of load; max and min are the maximum and minimum values of voltage.

2) LINE CURRENT CONSTRAINT IN POWER SYSTEM (APPROXIMATED BY BRANCH ANGLE CONSTRAINT)

Let $\theta_k^M = \alpha_i - \alpha_j$ be the voltage phase angle difference between nodes i and j at both ends of the branch, and the line current constraint of the power system is as follows:

$$\mathfrak{R}_{\theta r} := \mathfrak{R}_{\theta(TB)} \times \mathfrak{R}_{\theta(LB)} \tag{26}$$

Among them:

$$\mathfrak{R}_{\theta(TB)} := \left\{ \theta_{TB} \left| -\theta_{TB}^M \le \theta_{TB} \le \theta_{TB}^M \right. \right\} \tag{27}$$

$$\mathfrak{R}_{\theta(LB)} := \left\{ \theta_{LB} \left| -\theta_{LB}^M \le \theta_{LB} \le \theta_{LB}^M \right. \right\} \tag{28}$$

$$\theta_{TB} \in R^n, \quad \theta_{LB} \in R^{n_b - n} \tag{29}$$

where TB is the set of all branches, LB is the set of all connected branches.

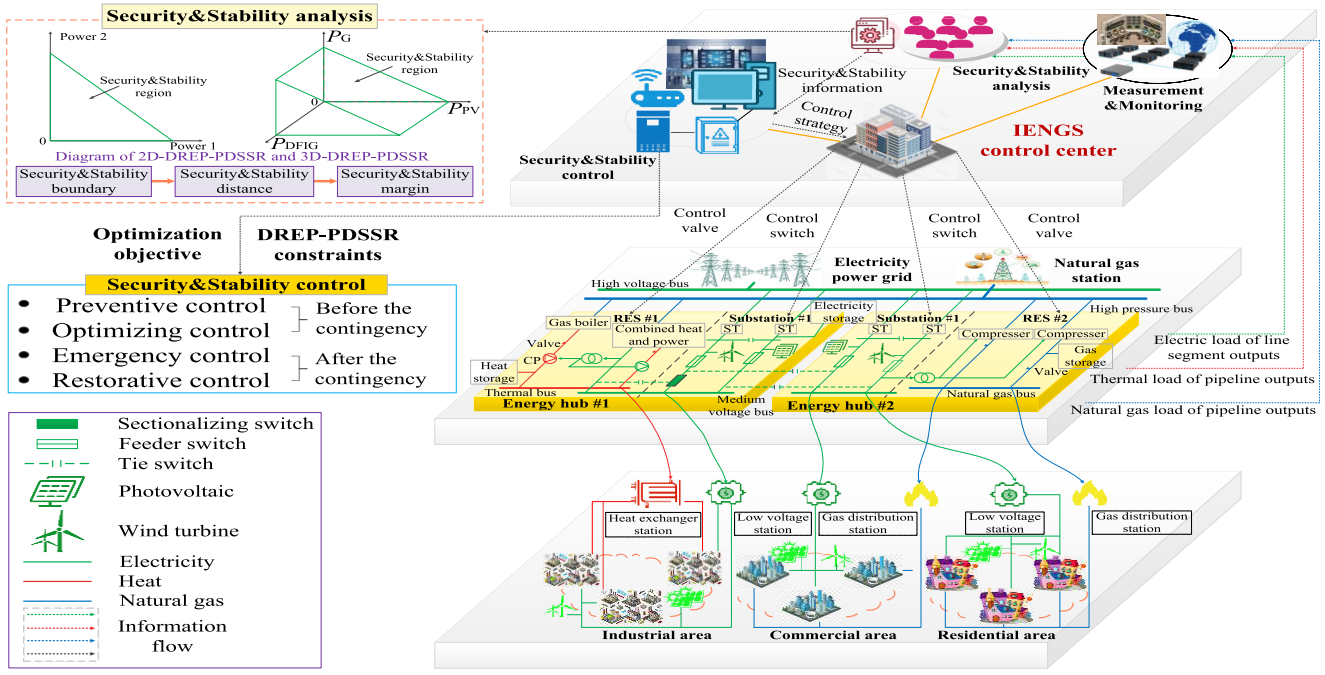

FIGURE 2. DREP-PDSSR security and stability analysis framework on the HRE-IENGS.

3) CONSTRAINTS OF ACTIVE POWER GENERATION EQUIPMENT IN POWER SYSTEM

If P_i^M and P_i^m represent the allowable upper and lower limits of active power P_i injected into generator bus i, the constraint set that can satisfy (V, θ) is as follows:

$$\mathfrak{R}_P := \left\{ (V,\theta) \,\middle|\, P_i^m \le P_i(V,\theta) \le P_i^M, i \in G \right\} \tag{30}$$

Among them:

$$V = \begin{pmatrix} V_G \\ V_L \end{pmatrix}, \quad \theta = \begin{pmatrix} \theta_{TB} \\ \theta_{LB} \end{pmatrix} \tag{31}$$

4) SECURITY CONSTRAINT SET OF POWER SYSTEM

The set $\mathfrak{R}$ defined in space (V, θ) is called the security constraint set, which can be expressed in equation (23). Among them:

$$\mathfrak{R}_{V(L)r} := \begin{cases} \Delta V_L \in R^{n-n_0} \\ V_L^m - V_L^0 \le \Delta V_L \le V_L^M - V_L^0 \end{cases} \tag{32}$$

$$\mathfrak{R}_{V(G)r} := \begin{cases} \Delta V_G \in R^{n_0} \\ V_G^m - V_G^0 \le \Delta V_G \le V_G^M - V_G^0 \end{cases} \tag{33}$$

where V^0 is the voltage amplitude of the node, the angle of each branch is θ^0 (the voltage phase angle difference between the two ends of each branch), and P is the active power injected into each node, then the above constraint set can be given in the incremental form.

B. PDSSR BOUNDARY OF POWER SYSTEM

Power system security and stability region is a node injection power space composed of active and reactive power injected by all nodes of the power system as shown in Fig. 3. Under the constraints of energy hub key equipment and critical line exit $N-1$, the system can operate safely. In the stable operating region of the power system, the relative relationship between the real-time operating point and the boundary of the security area can be observed, and the safe operation margin of the system can be monitored in real-time. When the system is not in safe operation mode, the load can be adjusted by adjusting the output of the feeder and main transformer, so that the operation point can return to the internal security area under the condition of minimum load shedding.

HRE-IENGS security and stability state transition are illustrated in Fig. 4. The boundary of dynamic security and stability margin is uniquely determined based on the network topology of the system and does not change with the operation state (such as node injection). For the given network topology and predetermined contingency, the DSSR boundary only needs to be calculated once, and its HP coefficient is stored in the database for on-line use in the future, without increasing the computational burden of on-line use. The high penetration of renewable energy is the development trend of the power grid in the future; however, the change of renewable energy penetration causes the change of the nature of the power grid, and the security and stability region of the power grid also changes accordingly. The security region can be used to analyze the stability of IENGS under different renewable energy permeability (DREP).

There are two hypotheses in the security region of the power system:

Hypothesis 1: The reactive power of the power system can be balanced locally, and the change of active power has little

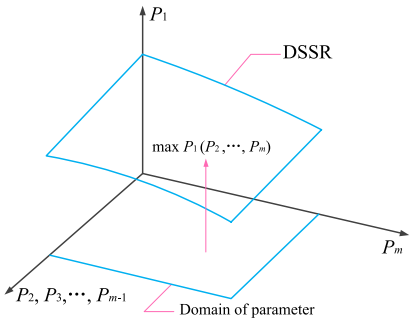

FIGURE 3. Parameterized optimization model of the DSSR.

effect on the voltage level, thus only the DSSR of active power needs to be studied.

Hypothesis 2: In the injected power space, because the active power injection of the generator is always positive and the active power injection of the load is always negative, the DSSR should satisfy the following inequality:

$$P_u \geq 0, \quad P_v \leq 0 \tag{34}$$

where u is the generator node-set and v are the load node-set.

Immediately after a large disturbance in the power system, all the pre-fault operating points in nodal power injection space, which can still guarantee the transient stability, constitute the DSR. When a short circuit fault occurs, configuration of the power system will go through three stages, which are pre-fault, fault-on, and post-fault, and the corresponding stage equation is:

$$\begin{cases} \dfrac{dx}{dt} = f_a(x), & -\infty < t < 0 \\ \dfrac{dx}{dt} = f_b(x), & 0 < t < \tau \\ \dfrac{dx}{dt} = f_c(x), & \tau < t < +\infty \end{cases} \tag{35}$$

where a, b and c represent configuration of pre-fault, fault-on and post-fault, respectively; τ is the fault duration.

For the injected power vector y (including the active power injection P_i of three units), the given power system topology is transient stable after a given short-circuit fault. This state is called power system dynamic security stability, and the injected power y is dynamically safe. The DSSR Ω_d (a, b, c) in the injected power space is as follows:

$$\Omega_d(a, b, c) := \{y \,|x_d(y) \in A(y)\} \cap Y_l \tag{36}$$

where $x_d(y)$ is the state at the moment of fault clearing; $A(y)$ is the stable region around the equilibrium point determined by injection y in the state space after the accident, and Y_l is the constraint set of upper and lower limits of injection power space of each node.

V. RESEARCH ON HYPERPLANE FITTING BASED ON DSADE-LSSVM METHOD

A. ESTABLISHMENT OF HYPERPLANE EQUATION

The methods to solve HP include the fitting method, dimension reduction method, reduction method, and intercept

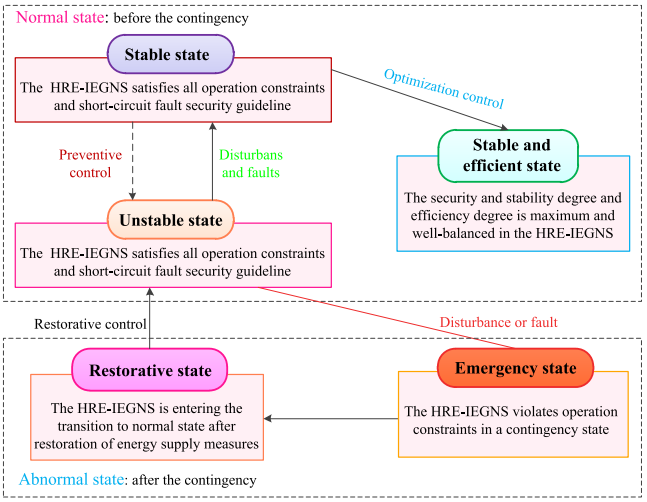

FIGURE 4. Illustration of HRE-IENGS stability state transition.

method. In this study, the intercept method and DSADE-LSSVM method were combined to calculate the HP coefficient of the security region, and then the PDSSR of HRE-IENGS system was obtained.

PDSSR is composed of critical HPs. The HP equation can be expressed as follows:

$$\sum_{s=1}^{n} \alpha_s P_s = 1 \tag{37}$$

where P_s is the s^{th} active power injection of the system; and α_s is the HP coefficient corresponding to P_s.

When the HP approximation is used to describe the boundary of the DSSR, the DSSR in the injected active power space is:

$$\Omega_d := \left\{ P \in R^n \left| \begin{array}{c} \sum_{s=1}^{n} \alpha_s P_s \leq 1 \\ P_s^m \leq P_s \leq P_s^M, s = 1, 2, \cdots, n \end{array} \right. \right\} \tag{38}$$

The fitting error of the PDSSR boundary is as follows:

$$Err_{PDSSR} = \frac{\left| \sum_{i=1}^{n} \alpha_i P_i - 1 \right|}{\sqrt{\sum_{i=1}^{n} \alpha_i^2} \bullet \sqrt{\sum_{i=1}^{n} P_i^2}} \tag{39}$$

Let max $(err_1, \ldots, err_t)$ represent the maximum fitting error. When the value is less than 5 %, the requirements of practical engineering application can be satisfied, and the smaller the value is, the higher the accuracy is.

B. DSADE ALGORITHM

Differential evolution (DE) algorithm [43] is a swarm intelligence optimization algorithm proposed by the American scholar storm and price to solve continuous space functions, which is suitable for solving optimization problems with a long search distance between initial solution and optimal

solution. It contains three main operations, i.e., mutation, crossover, and selection. In this study, in order to solve the dynamic optimization problem, a novel dynamic self-adaptive differential evolution algorithm (DSADE) was proposed by improving the DE algorithm. The performance of the DE algorithm is highly dependent on the parameter settings and the search gets in a local-optimal solution easily. To achieve good performance on a specific problem by using DE algorithms, some improvements are proposed. On the one hand, it can detect and timely respond to the environmental changes in dynamic optimization; on the other hand, it improves the global exploration ability and local development ability of differential evolution algorithm when the environment changes, improves the convergence speed of the algorithm, and prevents the algorithm from premature convergence and falling into local optimization. DSADE has recently been used for global optimization in such a broad area of problems such as scheduling [44], engineering design [45], constrained optimization problems [46], and others [47], [48]. DSADE is based on the population of D-dimensional parameter vectors. Compared to other evolutionary algorithms, DSADE also includes initialization, mutation, hybridization and selection. The difference is that DSADE has strong adaptive search ability by disturbing the basic individual with individual difference component. The decision vector $\boldsymbol{x}_i = [x_{i,1}, x_{i,2}, \ldots, x_{i,\mathrm{D}}]$ with D-dimensions can be regarded as an individual. The population, contains NP individuals, and is denoted by $\boldsymbol{X} = [\boldsymbol{x}_1, \boldsymbol{x}_2, \ldots, \boldsymbol{x}_{NP}]$. The evolution process is as follows:

(1) Initialization: set the size and members of the initial population, the maximum number of generations, the mutation parameter, and the crossover parameter.

(2) Mutation operation: the mutant individual is generated by one of six strategies. The difference between them is the way of individual selection (current individual, best individual and random individual). The six strategies are given as follows:

$$\text{“DDE/rand/1”} : v_i = x_{r1} + F \cdot (x_{r2} - x_{r3}) \tag{40}$$

$$\text{“DDE/rand/2”} : v_i = x_{r1} + F \cdot (x_{r2} - x_{r3}) + F \cdot (x_{r4} - x_{r5}) \tag{41}$$

$$\text{“DDE/best/1”} : v_i = x_{best} + F \cdot (x_{r2} - x_{r3}) \tag{42}$$

$$\text{“DDE/best/2”} : v_i = x_{best} + F \cdot (x_{r2} - x_{r3}) + F \cdot (x_{r4} - x_{r5}) \tag{43}$$

$$\text{“DDE/current} - \text{to} - \text{best/1”} : v_i = x_i + F \cdot (x_{best} - x_i) + F \cdot (x_{r1} - x_{r2}) \tag{44}$$

$$\text{“DDE/current} - \text{to} - \text{best/2”} : v_i = x_{bset} + F \cdot (x_{best} - x_i) + F \cdot (x_{r1} - x_{r2}) \tag{45}$$

where x_{best} is the superior individual; $x_{r1}, x_{r2}, x_{r3}, x_{r4}, x_{r5}$ are randomly selected from NP individuals; and F is the mutation parameter.

(3) Crossover operation: the individual is obtained probabilistically by

$$u_{i,j} = \begin{cases} v_{ij} & rand\ (0,\ 1) \le CR_i \\ x_{ij} & otherwise \end{cases} \quad j = 1, 2, \cdots, D \tag{46}$$

where CR is the crossover parameter.

(4) Selection operation: if the functional value of the offspring is better than that of the parent, the offspring replaces the parent, otherwise, the parent remains.

$$\hat{x}_i = \begin{cases} u_i & f\ (u_i) \le f\ (x_i) \\ x_i & f\ (u_i) \ge f\ (x_i) \end{cases} \quad i = 1, 2, \cdots, NP \tag{47}$$

(5) End: if the evolution process satisfies the termination conditions, the process is terminated; else, steps (2) – (4) are repeated.

C. LSSVM ALGORITHM

LSSVM is a modification of the standard support vector machine (SVM) and was developed by Suykens [49]. LSSVM is used for the optimal control of non-linear Karush–Kuhn–Tucker systems for classification as well as regression.

Considering the first a model in the primal weight space of the following form:

$$y(x) = \boldsymbol{w}^T \varphi(x) + b \tag{48}$$

where the $x \in \mathbb{R}^n$, $y \in \mathbb{R}$ and $\varphi(\cdot) : \mathbb{R}^n \to \mathbb{R}^{nh}$ are the mapping to the high dimensional feature space. Given a sample of the training set $\{x_i, y_i\}_{i=1}^{l}$ can be formulated then the following optimization problem is in the primal weight space. Still combining the functional complexity and fitting error, the optimization problem of LSSVM is given as:

$$\text{Min } J\ (\boldsymbol{w}, \xi) = \frac{1}{2}\boldsymbol{w}^T\boldsymbol{w} + y\frac{1}{2}\sum_{i=1}^{l}\xi_i^2 \tag{49}$$

$$\text{Such that: } y_i = \boldsymbol{w}^T\varphi\ (\mathbf{x}_i) + b + \xi_i \quad i = 1, 2, \cdots, l \tag{50}$$

Notably, this is in fact nothing else but a ridge regression cost function formulated in the feature space. However, one should be aware that when $\boldsymbol{w}$ becomes infinite-dimensional, this primal problem cannot be solved. This formulation consists of equality instead of inequality constraints. Constructing the lagrangian:

$$L\ (\boldsymbol{w}, b, \xi, \alpha) = J\ (\boldsymbol{w}, b, \xi) - \sum_{i=1}^{l}\alpha_i \left\{\boldsymbol{w}^T\varphi\ (\mathbf{x}_i) + b - y_i + \xi_i\right\} \tag{51}$$

where $\alpha_i \in R$ are the Lagrange multipliers, which can be positive or negative in LSSVM algorithm formulation. From the optimization conditions, the following equations must be

satisfied:

$$\begin{cases} \dfrac{\partial L}{\partial \boldsymbol{w}} = 0 \rightarrow \boldsymbol{w} = \sum_{i=1}^{l} \alpha_i \varphi\left(\mathbf{x}_i\right) \\ \dfrac{\partial L}{\partial b} = 0 \rightarrow \boldsymbol{w} = \sum_{i=1}^{l} \alpha_i = 0 \\ \dfrac{\partial L}{\partial \xi_i} = 0 \rightarrow \alpha_i = \gamma \xi_i \\ \dfrac{\partial L}{\partial i} = 0 \rightarrow \boldsymbol{w}^T \varphi\left(\mathbf{x}_i\right) + b - y_i + \xi_i = 0 \\ \quad For\ i = 1, 2, 3, \cdots, l \end{cases} \tag{52}$$

After elimination of the variables $\boldsymbol{w}$ and ξ one obtains the following matrix solution:

$$\begin{bmatrix} 0 & 1_v^T \\ 1 & \boldsymbol{\Omega} + \dfrac{1}{\gamma} I \end{bmatrix} \begin{pmatrix} a \\ b \end{pmatrix} = \begin{pmatrix} 0 \\ y \end{pmatrix} \tag{53}$$

with $y = [y_1, ..., y_l]$, $1_v = [1, ..., l]$, $\xi = [\xi_1, ..., \xi_l]$, $\alpha = [\alpha_1, \ldots, \alpha_l]$, Mercer's condition is applied within the $\boldsymbol{\Omega}$ matrix:

$$\boldsymbol{\Omega}_{ij} = y_i y_j \varphi\left(\mathbf{x}_i\right)^T \varphi\left(\mathbf{x}_i\right) = y_i y_j K\left(\mathbf{x}_i, \mathbf{x}_j\right) \tag{54}$$

The fitting function namely the output of LSSVM regression is represented as follows:

$$y\left(x\right) = \sum_{i=1}^{l} a_i K\left(\mathbf{x}_i, \mathbf{x}_j\right) + b \tag{55}$$

where α_i and b are the solutions to the linear system. Although the choices of the kernel function $K\left(\mathbf{x}_i, \mathbf{x}_j\right)$ in LSSVM are the same as those in SVM, more emphasis has been put on the powerful RBF kernel. Noteworthy in the case of RBF Kernel, one has only two additional tuning parameters which are γ, σ and δ_2 as a bandwidth kernel:

$$K\left(x_i, x_j\right) = \exp\left(-\frac{\|x - x_i\|^2}{\delta^2}\right) \tag{56}$$

D. FILE FORMATS FOR GRAPHICS DSADE-LSSVM TO SOLVE PDSSR BOUNDARY

For the security and stability region of the power system under DREP, only the calculation of the PDSSR is required under each DREP once, and its parameters (HP coefficient, security stability region map) are stored in the database. Furthermore, it can be called directly when necessary, which can realize off-line calculation and on-line application. It does not increase the computational burden of on-line use. For a given operating point of renewable energy permeability, finding the corresponding security stability region map can judge whether the system is in a safe state at that time. It is unstable outside the region, critical stability at the boundary of the security region, and complete stability in the region.

A group of individuals with high fitness could be obtained by using the DSADE algorithm. Furthermore, LSSVM was used to approach the optimal solution of the original constrained optimization problem step by step in the feasible region. Therefore, combining the advantages of the two algorithms, DSADE-LSSVM was proposed to solve the PDSSR. The flow chart of the algorithm is presented in Fig. 5. The simulation initialization population is 200, the crossover probability is 0.9, and the maximum number of iterations is 1000. The dimension of solving the problem is set as 3D, and the individuals with large fitness correspond to the output. Then, the search direction and the number of critical points were set to store the critical operation points each time, and critical points were obtained for fitting.

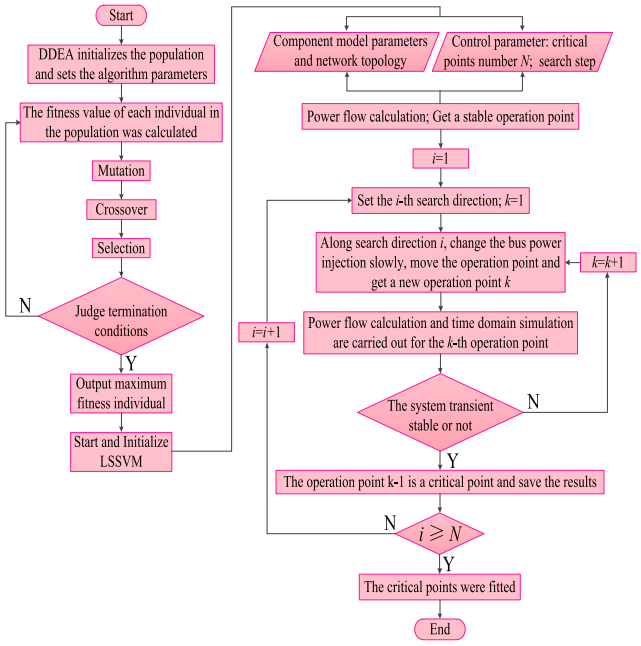

FIGURE 5. DSADE-LSSVM flow chart for solving security stability region.

VI. CASE STUDY

With the increasing penetration of RE, the security and stability of the power system are significantly affected. Wind power, PV power and conventional gas-power system are three completely different power forms, and their dynamic characteristics are different from each other. Therefore, it is necessary to study the three energy forms to form a 3D PDSSR, which can reflect the real-time operation state of the system. In this study, the DSSR of a power system with different permeability of RE was studied. The active power output of wind power, PV power and conventional gas-power system were considered as three independent variables to study the influence of the three factors on the HRE-IENGS system. The security and stability limit of the system were also the stable operation boundary determined by three independent variables.

A. DSADE-LSSVM TO SOLVE DREP-PDSSR

In the past, no research was conducted on DSSR for the power system with both wind power and PV power. Therefore, the fitting method with high precision and a large amount

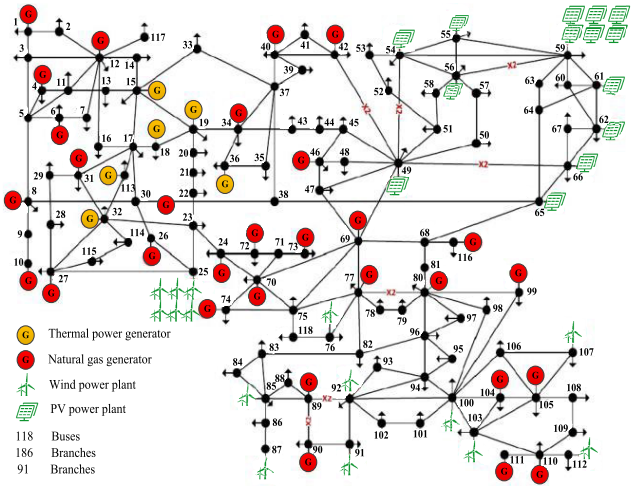

FIGURE 6. IEEE new England 118 bus system.

TABLE 1. DREP-PDSSR hyperplane coefficient is determined.

DREP	G89 hyperplane coefficients	DFIG hyperplane coefficients	PV hyperplane coefficients
5 %	-15	4.579 1	0.182 8
10 %	-15	8.433 1	0.367 7
15 %	-15	12.06	0.592 2
20 %	14.769 7	-15	-0.859 7
25 %	11.624 7	-15	-0.912 4
30 %	9.325	-15	-0.951 3
35 %	7.275 5	-15	-0.953 7
40 %	-5.69 2	15	0.945 5
45 %	7.928 7	15	-1.063 6
50 %	7.272 6	15	-1.193 4

of calculation was used to obtain DREP-PDSSR, when the topological properties of the DSSR boundary were unknown. The IEEE 118 bus system shown in Fig. 6 was used to analyze DREP-PDSSR. In the simulation, the wind power plant is connected to bus 25, which is a doubly-fed induction generator (DFIG) 5 MW wind turbine. In bus 59, a PV power station is used to replace the traditional power unit, which is 3 PH 0.5 MW PV unit. A three-phase short-circuit fault is set at the neutral point of bus 30 (500 kV) of the IEEE 118 system. The time of starting fault is 3 s, the time to remove the three-phase short circuit fault is 3.1 s, and the fault lasts for 0.1 s. In the simulation process, the reference capacity is taken as 100 MW. When solving the DREP-PDSSR, the active power ratio of wind power is about 2 times that of PV power.

1) SOLUTION OF HYPERPLANE COEFFICIENT BASED ON DSADE-LSSVM METHOD

First, a series of operation points were calculated according to DSADE-LSSVM under the constraint of HP, and the optimal HP coefficient was obtained. In this study, the permeability was set as 10 gradients, the increment was 5 %, and the initial permeability was 5 %. Ten groups of HP coefficients are obtained. The calculation results are listed in Table 1.

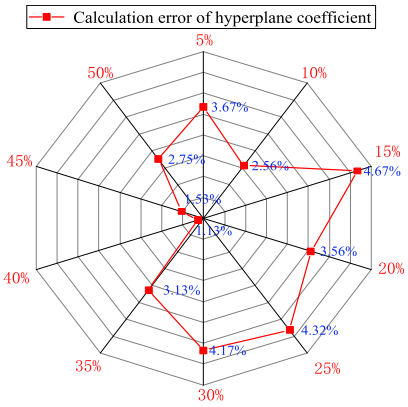

FIGURE 7. Calculation error of HP coefficient.

The absolute value of the HP coefficient presented in Table 1 represents the influence of the active power injection point of three buses in the system DSSR. Clearly, the output change of traditional power has the greatest impact on the system. With the increase of permeability, the influence degree of wind power gradually increases, and the impact factor of PV power is relatively small than those of the other two energy sources. The calculation error of the HP coefficient under DREP of 5 to 50 % is shown in Fig. 7. When the permeability is 40 and 50 %, there are high accuracy and reliability of the fitting plane, which is the smallest error of the HP coefficient.

The maximum error of PDSSR boundary hyperplane obtained by fitting is 4.67 % (the error here is defined as the maximum value of the ratio of each coordinate component of the distance from the critical point to the fitting hyperplane to each coordinate component of the corresponding point on the hyperplane, which is a percentage). All the results meet the accuracy requirements of engineering.

2) SOLUTION OF HYPERPLANE COEFFICIENT BASED ON DSADE-LSSVM METHOD

After the fault occurs, the active power output of the four units decreases suddenly, the reactive power output increases and the voltage decreases. After the fault is removed, the active power output and the voltage increase, and the reactive power output decreases. The active power output of each unit is shown in Fig. 8.

Fig. 8 demonstrates that the recovery speed of each power unit from fast to slow is in the following order. The recovery time of traditional synchronous generator, natural gas generator, wind power, and PV power are 6.1, 0.118, 0.16, and 0.38 respectively.

B. FITTING AND ANALYSIS OF SYSTEM DREP-PDSSR

1) 3D- DREP-PDSSR FITTING OF THE SYSTEM

Through a large amount of simulation calculation, it was found that the boundary of DREP-PDSSR could be fitted by the HP method, and the error could be maintained within the allowable range of engineering. Several operation points near

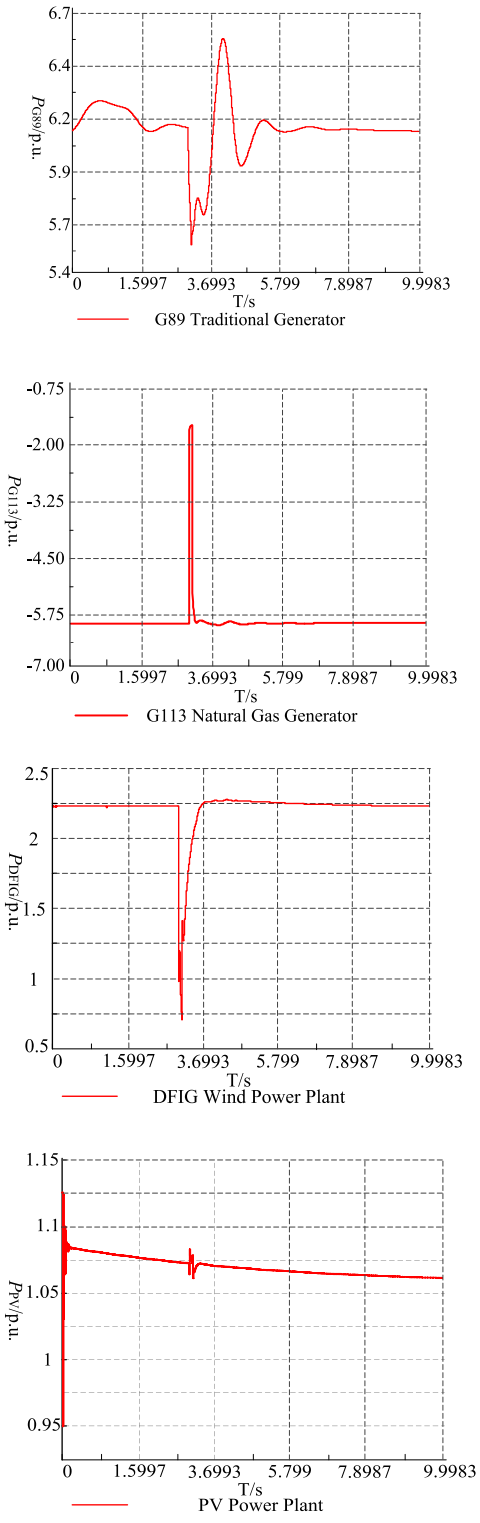

FIGURE 8. The active power distribution of each generator faults.

the boundary were selected for time-domain simulation, and the security and stability domain boundary is verified. The HP coefficients determined by using the DSADE-LSSVM and

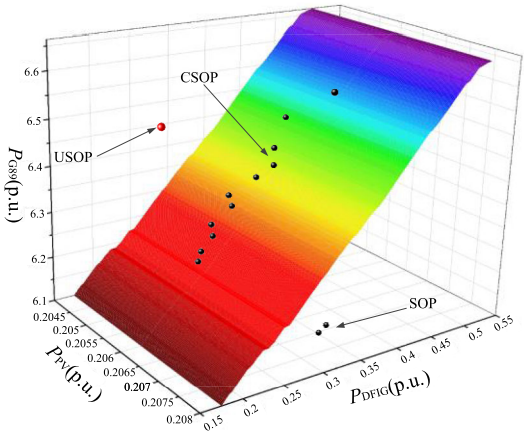

FIGURE 9. DREP-PDSSR at 5 % permeability.

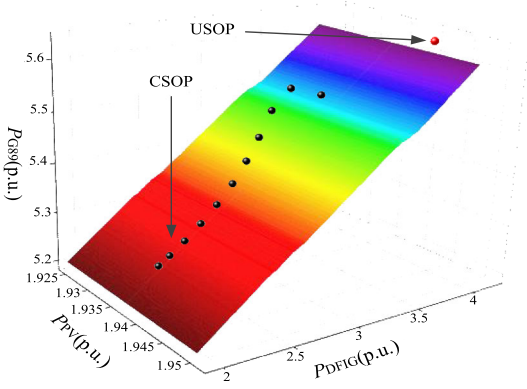

FIGURE 10. DREP-PDSSR at 50 % permeability.

DIgSILENT/Power Factory simulation were used to obtain the active power output of the three types of power generation to fit DREP-PDSSR. Among them, the 3D PDSSR with renewable energy permeability of 5 to 50 % (i.e. the maximum and minimum permeability) are shown in Figs. 9 and 10. The DREP-PDSSR obtained is the critical boundary of PDSSR fitted when a three-phase short circuit fault occurred in bus 30, and the DREP-PDSSR under other permeability conditions is shown in the Appendix. The unstable operation point (USOP), the critical stable operation point (CSOP), and the stable operation point (SOP) are clearly shown in the figure, respectively.

Furthermore, some operation points near the DREP-PDSSR boundary were selected for time-domain simulation to judge whether the operation points were transient stable or not and whether they were located in the security and stability region to improve the accuracy of dynamic security and stability region boundaries. The results of active power injection and time-domain simulation at the operating point for when the 5 and 50 % renewable energy permeability are presented in Tables 2 and 3.

TABLE 2. Time domain simulation results of 5 % permeability.

Operation point	P_{G89} (MW)	P_{DFIG} (MW)	P_{PV} (MW)	secure or not	Time-domain simulation
1	667.785 532	25.092 417	10.709 415	N	Unstable
2	654.433 021	12.973 317	10.661 121	Y	stable
3	649.580 488	13.013 978	10.778 405	Y	stable
4	643.563 881	15.242 056	10.747 255	Y	stable
5	638.497 184	14.461 561	10.746 176	Y	stable
6	629.566 52	9.490 373	10.725 492	Y	stable
7	625.457 871	8.509 135	10.732 786	Y	stable
8	621.527 722	7.936 915	10.714 979	Y	stable
9	617.769 091	7.559 553	10.718 454	Y	stable
10	633.879 102	11.276 494	10.745 077	Y	stable

TABLE 3. Time domain simulation results of 50 % permeability.

Operation point	P_{G89} (MW)	P_{DFIG} (MW)	P_{PV} (MW)	secure or not	Time-domain simulation
1	562.276 585	45.889 068	19.491 825	N	Unstable
2	556.421 023	35.618 017	19.381 521	Y	stable
3	554.305 216	34.613 078	19.357 845	Y	stable
4	549.288 512	31.254 561	19.367 385	Y	stable
5	543.152 187	28.228 019	19.376 157	Y	stable
6	539.266 237	27.008 195	19.378 537	Y	stable
7	535.567 921	25.208 193	19.382 059	Y	stable
8	532.220 301	24.396 174	19.405 159	Y	stable
9	527.857 529	22.627 017	19.411 055	Y	stable
10	523.886 068	19.976 097	19.445 107	Y	stable

In order to further verify the accuracy of the proposed method, a small range $\sum_{i=1}^{n} a_i P_i \leq 1$ around the PDSR boundary $\sum_{i=1}^{n} a_i P_i = 1$ is set. A number of operating points in this range are selected randomly and the PDSR boundary obtained by the proposed method and time-domain simulation is used to judge whether each selected operating point is transient stable. For the given selected operating point, if $\sum_{i=1}^{n} a_i P_i$ is smaller than 1, the point is inside the boundary and transient stable; if $\sum_{i=1}^{n} a_i P_i$ is larger than 1, the point is not inside the boundary and transient unstable. Tables 2 and 3, summarize that under the same calculation conditions, operation point 1 is unstable under the time-domain simulation of 5 and 50 % permeability (operation points outside the 3D DREP-PDSSR domain in Fig. 3), which does not meet the transient stability constraints. When renewable energy permeability is 20 % or less, the impact on the system is relatively small; however, the impact of wind power is always greater than that of PV power. With the increase of renewable energy penetration of power systems, the impact of wind power becomes more and more serious, and the impact of PV power also increases; nonetheless, the increasing trend is not obvious. Comparative analysis of system operation indexes presented in Table 4 indicates that with the increase of renewable energy permeability, the stable operation points increase, the boundary of security region expands, the simulation convergence speed accelerates, the power supply recovery time after the expected fault decreases and the recovery speed accelerates, which proves the high accuracy of PDSR boundary obtained by the proposed method.

C. SENSITIVITY ANALYSIS

The sensitivity analysis was carried out according to the number of safe and stable operation points obtained in 3D-PDSSR space. In this study, it was assumed that the change rates of active power values at all stable operation points are

TABLE 4. System performance index DREP.

renewable energy permeability	Number of operation points in the security region	Convergence rate of time-domain simulation (s)	Power supply recovery speed after failure (s)	Number of stable operation points in time-domain simulation
5%	9	3.798 7	0.698 3	9
10%	11	3.695 8	0.687 3	11
15%	13	3.625 4	0.663 2	13
20%	14	3.598 6	0.658 2	14
25%	15	3.495 5	0.657 9	15
30%	17	3.462 1	0.638 3	17
35%	18	3.394 3	0.623 6	18
40%	19	3.318 6	0. 598 3	19
45%	21	3.125 6	0.543 6	21
50%	23	3.001 8	0.494 1	23

30, 20, 10, – 10, – 20, and – 30 %, respectively. Then the active power value of the safe and stable operation point is recalculated, and the position of the point in the security and stability region is analyzed and judged. Fig. 11 shows the number of safe and stable operation points under DREP.

Fig. 11 exhibits that fluctuation and a slight decrease in the number of safe and stable operation points in the range of 45-50 % and 5-20 %. However, the number of safe and stable operation points of 25-40 % remains relatively stable. When the renewable energy is just connected with a large number of access points, the intermittent characteristics of renewable energy and the simultaneous access of a large number of power electronic equipment affect the number of safe and stable operation points of the system. Although the number of safe and stable operation points fluctuated slightly, the overall trend of safe and stable operation points increased with the permeability of RE.

D. COMPARISON ANALYSIS

To evaluate the effectiveness of DSADE by comparing it with two other well-known meta-heuristics including, genetic

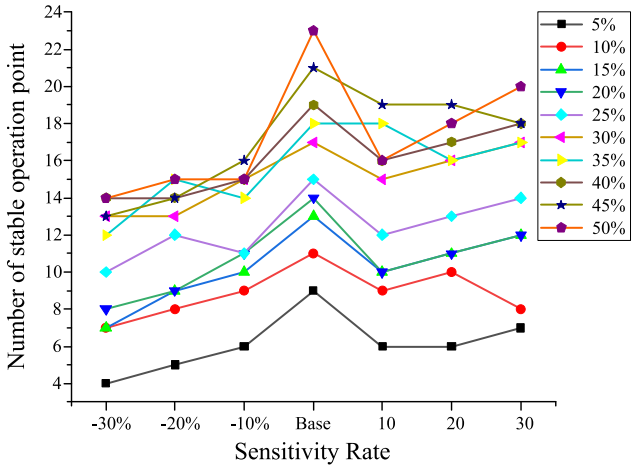

FIGURE 11. Sensitivity analysis of stable operation point in DREP.

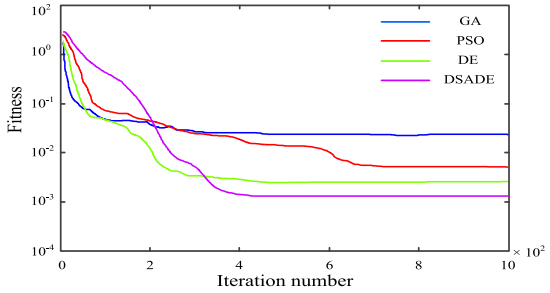

FIGURE 12. The average convergence accuracy.

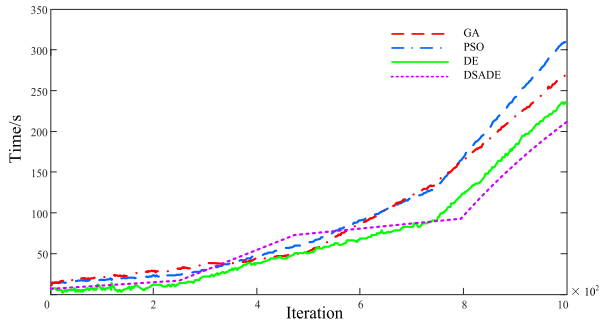

FIGURE 13. Iteration time of algorithms.

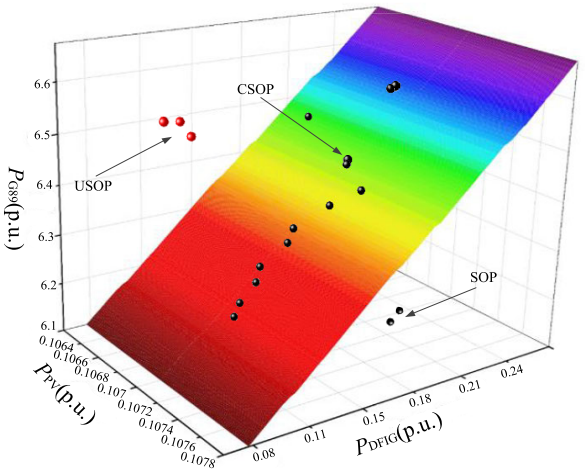

FIGURE 14. DREP-PDSSR at 10 % permeability.

TABLE 5. Control parameters of all algorithms.

Methods	Parameters	Value
GA	Crossover probability	0.9
	Mutation probability	0.01
PSO	Inertia weight, w	-0.3236
	Particle's best weight, c1	-0.1136
	Swarm's best weight, c2	3.9789
DE	Mutation factor, F	0.5
	Crossover factor, CR	0.9

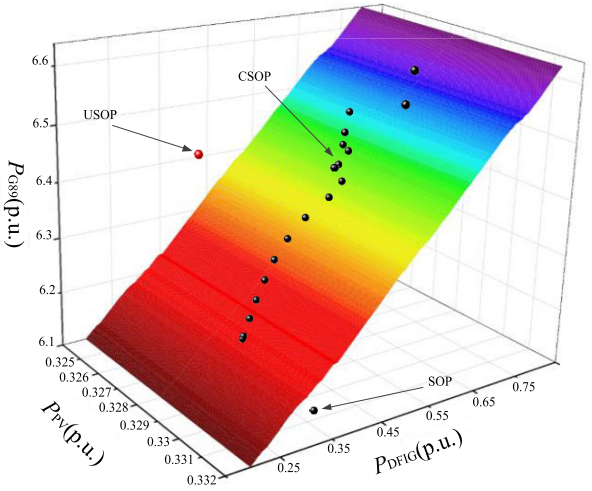

FIGURE 15. DREP-PDSSR at 15 % permeability.

algorithm (GA), particle swarm optimization (PSO) algorithm. During experimentation, control parameters of all algorithms are set as Table 5. Where, GA algorithm uses a single point crossover, uniform selection, and uniform mutation. DE and PSO algorithm are set as follows based on Price (1997) and Rao (2016), respectively.

To assess the performance and feasibility of the proposed DSADE method in DSSR fitting, the error and convergence accuracies of the three algorithms are compared and analyzed by using the simulation results. Fig. 12 shows the average convergence accuracy of DSADE, PSO and GA in the optimization. The DSADE, PSO, GA and DE parameters which are selected by the error method are included in Table 6.

Fig. 12 compares the fitness convergence of GA, PSO, and proposed the DE algorithm. The comparative results of the fitness convergence of GA, PSO and proposed DE strongly demonstrate that the proposed DE gives a better convergence performance than the other standard GA and PSO methods. The training results using the DE algorithm quickly converge after 400th generations meanwhile the results of the PSO algorithm only converge after up to 800th generations. The

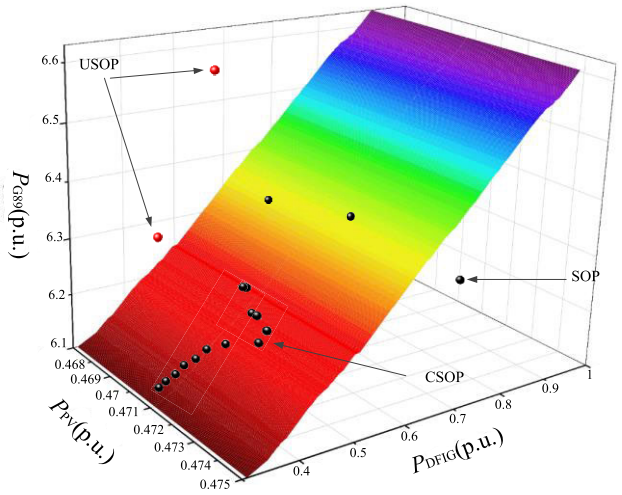

FIGURE 16. DREP-PDSSR at 20 % permeability.

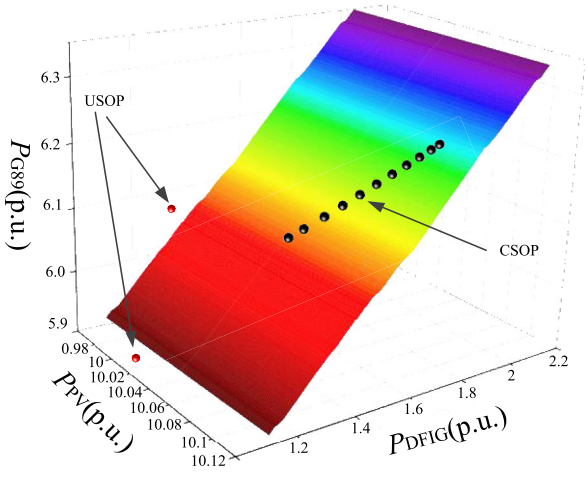

FIGURE 19. DREP-PDSSR at 35 % permeability.

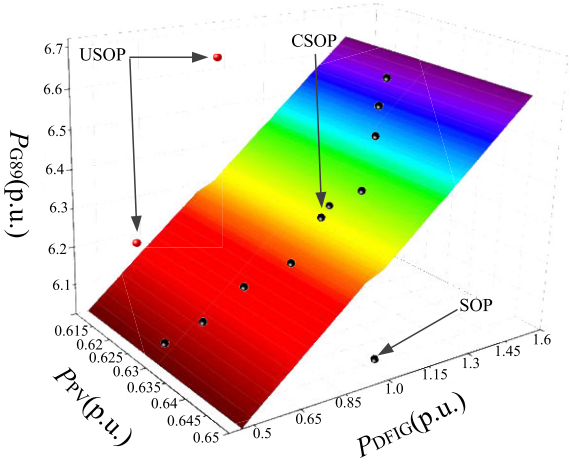

FIGURE 17. DREP-PDSSR at 25 % permeability.

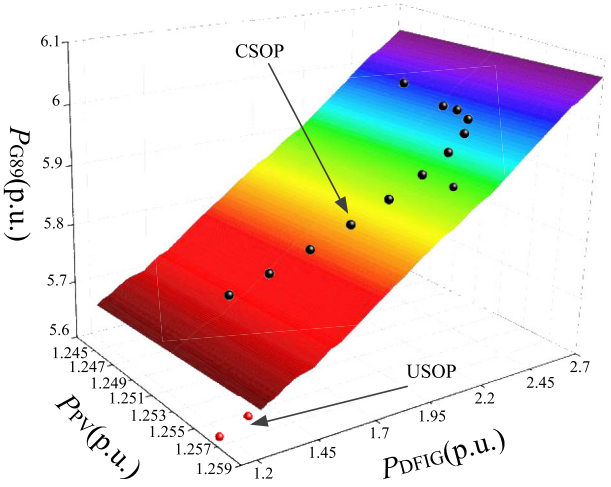

FIGURE 20. DREP-PDSSR at 40 % permeability.

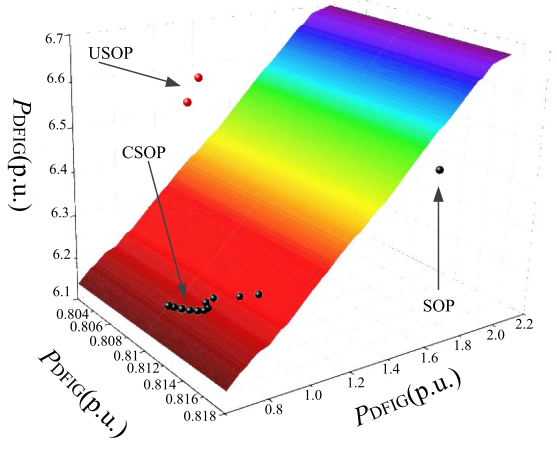

FIGURE 18. DREP-PDSSR at 30 % permeability.

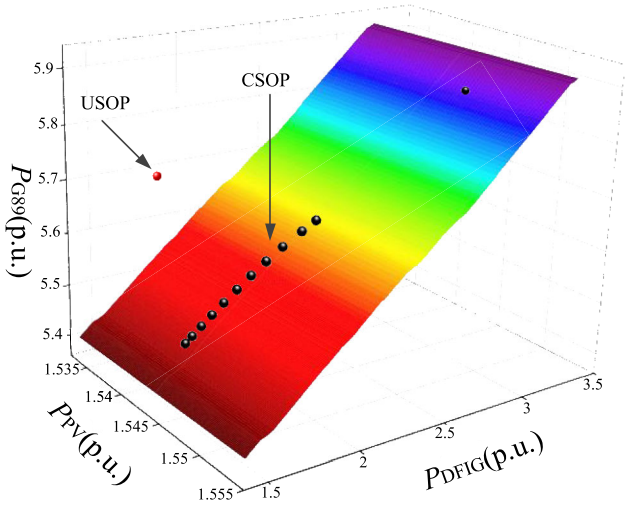

FIGURE 21. DREP-PDSSR at 45 % permeability.

GA eventually seems to be the most sluggish and required more time to be able to successfully converge. Then it is reasonable to say the SADE algorithm has well efficiency, which has stronger exploring capacity, overcoming premature convergence effectively and keep the speed of convergence.

TABLE 6. Control parameters of all algorithms.

Algorithms		MSE			
		Best	Worst	Average	Std. Dev
GA	5 %	0.0035	0.0280	0.0167	0.0082
	10 %	0.2802	74.8480	6.2886	33.0501
	15 %	2.39e-05	0.1079	0.0365	0.0321
	20 %	7.92e-05	4.21e-04	1.98e-04	1.14e-04
	25 %	1.38e+03	2.80e+03	2.02e+03	4.74e+02
	30 %	5.52e-05	9.90e-04	4.19e-04	2.38e-04
	35 %	0.8087	94.2039	28.0175	34.5246
	40 %	1.10e-30	2.58e-13	2.59e-14	8.17e-14
	45 %	1.20e-21	1.68e-20	6.92e-21	5.01e-21
	50 %	4.24e-47	1.13e-45	4.56e-46	3.39e-46
PSO	5 %	1.9996	7.0160	1.4938	5.1437
	10 %	1.0553	3.2639	1.4438	0.6579
	15 %	0.4160	3.4624	2.1448	1.1102
	20 %	1.50e+02	6.94e+03	1.07e+03	2.08e+03
	25 %	2.86e+03	5.45e+03	4.27e+03	6.38e+02
	30 %	0.7210	7.3193	3.3746	2.3257
	35 %	4.0406	1.20e+03	3.95e+02	4.43e+02
	40 %	1.01e-25	2.78e-06	3.10e-07	8.75e-07
	45 %	0.0043	2.4160	0.2527	0.7601
	50 %	0.0012	0.3378	0.1059	0.1330
DE	5 %	2.80e-12	1.09e-11	6.19e-12	2.31e-12
	10 %	7.21e-06	2.41e-05	1.19e-05	5.39e-06
	15 %	1.03e+03	6.69e-08	6.69e-09	2.11e-08
	20 %	6.15e-24	9.21e-23	4.03e-23	2.85e-23
	25 %	2.54e-04	2.55e-04	2.54e-04	4.19e-07
	30 %	3.11e-24	4.36e-23	1.53e-23	1.32e-23
	35 %	0.0037	15.4526	2.3702	4.9007
	40 %	-9.6601	-9.6134	-9.6501	0.0182
	45 %	-9.6601	8.9869	-9.5461	0.2545
	50 %	-9.1140	-7.8072	-8.4778	0.3489
DSADE	5 %	4.44e-15	1.20e-21	6.92e-21	1.49e-32
	10 %	4.24e-47	4.56e-46	3.39e-46	1.13e-45
	15 %	2.45e+04	3.69e+19	1.28e+48	1.31e+33
	20 %	1.95e-38	2.14e-27	1.20e-15	1.45e-05
	25 %	1.78e39	2.55e-23	4.19e-26	1.62e-67
	30 %	3.35e-02	2.03e-14	3.26e-01	1.46e-24
	35 %	3.37e-40	4.99e-30	2.65e-23	2.64e-62
	40 %	4.87e+41	0.0019	3.78e+05	3.16e+84
	45 %	5.09e-19	0.1059	3.31e-02	2.38e-02
	50 %	4.63e-03	3.46e-37	3.10e52	2.80e-03

The numerical results are given in Table 6, where ''Average'' and ''Std. Dev'' denote the average solution and standard deviation of the active power obtained over searching space. The GA and PSO fails to find the optimal solution for all problems. DE can obtain the optimal solution for all problems. The proposed DSADE algorithm has the best performance and outperforms compared with those of PSO, GA, and DE algorithms. The results indicate that the optimal solutions (Best) determined by DSADE are more advanced than those found by other methods in the mentioned test systems. The simulation confirms that DSADE is well capable of searching for the global or near-global optimum solution. Besides, the lower Std. Dev., which proves DSADE has a stable consistency and a refined convergence precision. In addition, the average global or near-global optimum solutions (Mean) result in stable average active power attained by DSADE, which is evidence for the reliability of DSADE with a high-quality solution. Moreover, the DSADE is more stable than DE with the smallest standard deviation for all problems.

As shown in Fig. 13, the iteration of the DSADE is faster than those of DE, GA and PSO algorithms. In summary, the results show that the proposed DSADE algorithm not only has a higher accuracy but also has a much faster convergence speed than those of DE, GA, and PSO algorithms. The DSADE also improve the accuracy of the stable operation region compared to the DE, significantly.

VII. CONCLUSION

This paper proposes the concept and model of the integrated energy system dynamic security and stability region. Considering the fact that the operating parameters could be maintained within the constraints in the urban regional integrated energy system, the practical integrated energy system dynamic security and stability region where operation parameter verifications are simplified was further established, which could improve the calculation speed. Then, a security and stability analysis framework for a regionally integrated energy system based on the dynamic security and stability region was given. Based on the practical dynamic security and stability region, the model of optimizing control is presented to adjust the system security status. The case study verifies the effectiveness of the practical security region and realizes its visualization in three-dimensional space. Furthermore, the secure operating point could be optimized to better security and efficiency status under the optimizing control.

The guidance of security region for energy field mainly reflects in the characteristics of security region boundary, shape, size and other indicators, which can be used as the basis for integrated energy system evaluation or optimization. Due to the dynamic security and stability region, some fields of integrated energy system research such as planning, operation, control could be carried out with security analysis quickly. In particular, the dynamic security and stability region could be visualized on two-dimensional or three-dimensional space. This visual characteristic helps to determine the security status of an operation point intuitively by observing whether the point lies in the region. Furthermore, it can balance the demands of system security and efficiency, and find the balance optimal state. Meanwhile, because the calculation of dynamic security and dynamic security and stability region was only related to the system topology and parameters that were independent of load state, dynamic security and stability region could be calculated off-line and applied on-line. Therefore, the DSSR has strong real-time application potential.

It should be noted that the richer security control model considering control cost and the shortest path will be researched and discussed in the next stage. Furthermore, energy storage systems and renewable energy resources are an important part of energy hubs. The integrated energy system dynamic security and stability region model considering the above factors will also be researched in the subsequent article.

APPENDIX

See Figs. 14–21.

REFERENCES

[1] J. Wu, J. Yan, H. Jia, N. Hatziargyriou, N. Djilali, and H. Sun, "Integrated energy systems," *Appl. Energy*, vol. 167, pp. 155–157, Apr. 2016, doi: 10.1016/j.apenergy.2016.02.075.

[2] G. Li, R. Zhang, T. Jiang, H. Chen, L. Bai, and X. Li, "Security-constrained bi-level economic dispatch model for integrated natural gas and electricity systems considering wind power and power-to-gas process," *Appl. Energy*, vol. 194, pp. 696–704, May 2017, doi: 10.1016/j.apenergy.2016.07.077.

[3] Y. Li, W. Liu, M. Shahidehpour, F. Wen, K. Wang, and Y. Huang, "Optimal operation strategy for integrated natural gas generating unit and power-to-gas conversion facilities," *IEEE Trans. Sustain. Energy*, vol. 9, no. 4, pp. 1870–1879, Oct. 2018, doi: 10.1109/TSTE.2018.2818133.

[4] T. Li, M. Eremia, and M. Shahidehpour, "Interdependency of natural gas network and power system security," *IEEE Trans. Power Syst.*, vol. 23, no. 4, pp. 1817–1824, Nov. 2008, doi: 10.1109/TPWRS.2008.2004739.

[5] J. Wang, J. Xu, S. Liao, and L. Sima, "Coordinated optimization of integrated electricity-gas energy system considering uncertainty of renewable energy output," *Automat. Elect. Power Syst.*, vol. 43, no. 15, pp. 2–9, 2019, doi: 1000-1026(2019)43:15<2:JJXNYC>2.0.TX.2-Q.

[6] A. Alabdulwahab, A. Abusorrah, X. Zhang, and M. Shahidehpour, "Coordination of interdependent natural gas and electricity infrastructures for firming the variability of wind energy in stochastic day-ahead scheduling," *IEEE Trans. Sustain. Energy*, vol. 6, no. 2, pp. 606–615, Apr. 2015, doi: 10.1109/TSTE.2015.2399855.

[7] X. Zhang, M. Shahidehpour, A. Alabdulwahab, and A. Abusorrah, "Hourly electricity demand response in the stochastic day-ahead scheduling of coordinated electricity and natural gas networks," *IEEE Trans. Power Syst.*, vol. 31, no. 1, pp. 592–601, Jan. 2016, doi: 10.1109/TPWRS.2015.2390632.

[8] C. He, L. Wu, T. Liu, and Z. Bie, "Robust co-optimization planning of interdependent electricity and natural gas systems with a joint N-1 and probabilistic reliability criterion," *IEEE Trans. Power Syst.*, vol. 33, no. 2, pp. 2140–2154, Mar. 2018, doi: 10.1109/TPWRS.2017.2727859.

[9] C. Wang, W. Wei, J. Wang, F. Liu, F. Qiu, C. M. Correa-Posada, and S. Mei, "Robust defense strategy for gas–electric systems against malicious attacks," *IEEE Trans. Power Syst.*, vol. 32, no. 4, pp. 2953–2965, Jul. 2017, doi: 10.1109/TPWRS.2016.2628877.

[10] M. Chertkov, S. Backhaus, and V. Lebedev, "Cascading of fluctuations in interdependent energy infrastructures: Gas-grid coupling," *Appl. Energy*, vol. 160, pp. 541–551, Sep. 2015, doi: /10.1016/j.apenergy.2015.09.085.

[11] X. Xu, H. Jia, H.-D. Chiang, D. C. Yu, and D. Wang, "Dynamic modeling and interaction of hybrid natural gas and electricity supply system in microgrid," *IEEE Trans. Power Syst.*, vol. 30, no. 3, pp. 1212–1221, May 2015, doi: 10.1109/TPWRS.2014.2343021.

[12] A. Martinez-Mares and C. R. Fuerte-Esquivel, "A unified gas and power flow analysis in natural gas and electricity coupled networks," *IEEE Trans. Power Syst.*, vol. 27, no. 4, pp. 2156–2166, Nov. 2012, doi: 10.1109/TPWRS.2012.2191984.

[13] C. Fuerte-Esquivel and A. Martinez-Mares, "A robust optimization approach for the interdependency analysis of integrated energy systems considering wind power uncertainty," in *Proc. IEEE PES Gen. Meeting | Conf. Expo.*, National Harbor, MD, USA, Jul. 2014, p. 1, doi: 10.1109/PESGM.2014.6938792.

[14] Z. Qiao, Q. Guo, and H. Sun, "Research survey on the modeling, planning and operational analysis of electricity-natural gas coupling system static security constraints," *J. Global Energy Interconnection*, vol. 3, no. 1, pp. 14–26, Jan. 2020, doi: 10.19705/j.cnki.issn2096-5125.2020.01.002.

[15] Z. Jiao, F. Ma, and Z. Li, "Study on combined operation of gas-electricity coupling system and emergency overload control considering the characteristics of natural gas," *Proc. CSEE*, vol. 39, pp. 77–83, Sep. 2019. [Online]. Available: http://www.pcsee.org/CN/Y2019/V39/Izk/77

[16] B. Luo, Y. Mu, W. He, and X. Yu, "Load supply capability assessment method for integrated electricity-gas system considering," *J. Global Energy Interconnection*, vol. 3, no. 1, pp. 14–26, Jan. 2020, doi: 10.19705/j.cnki.issn2096-5125.2020.01.002.

[17] C. M. Correa-Posada and P. Sanchez-Martin, "Security-constrained optimal power and natural-gas flow," *IEEE Trans. Power Syst.*, vol. 29, no. 4, pp. 1780–1787, Jul. 2014, doi: 10.1109/TPWRS.2014.2299714.

[18] W. Gan, X. Ai, J. Fang, W. Yao, W. Zuo, J. Wen, and M. Yan, "Security constrained co-planning of transmission expansion and energy storage," *Appl. Energy*, vol. 239, pp. 383–394, Apr. 2019, doi: 10.1016/j.apenergy.2019.01.192.

[19] L. Liu, D. Wang, H. Jia, and S. Li, "Security region model for regional integrated energy system," *Elect. Power Automat. Equip.*, vol. 38, no. 8, pp. 63–71, 2019, doi: 1006-6047(2019)39:8<63:MXQYZH>2.0.TX.2-H.

[20] H. D. Nguyen, K. Dvijotham, and K. Turitsyn, "Constructing convex inner approximations of steady-state security regions," *IEEE Trans. Power Syst.*, vol. 34, no. 1, pp. 257–267, Jan. 2019, doi: 10.1109/TPWRS.2018.2868752.

[21] J. Z. Zhu, R. Fan, G. Xu, and C. S. Chang, "Construction of maximal steady-state security regions of power systems using optimization method," *Elect. Power Syst. Res.*, vol. 44, no. 2, pp. 101–105, Feb. 1998, doi: 10.1016/S0378-7796(97)01188-7.

[22] H. Sharifzadeh, N. Amjady, and H. Zareipour, "Multi-period stochastic security-constrained OPF considering the uncertainty sources of wind power, load demand and equipment unavailability," *Electr. Power Syst. Res.*, vol. 146, pp. 33–42, May 2017, doi: 10.1016/j.epsr.2017.01.011.

[23] S. J. Chen, C. Q. Kang, Q. Xia, and Q. X. Chen, "Steady-state security assessment method based on distance to security region boundaries," *IET Gener., Transmiss. Distrib.*, vol. 7, no. 3, pp. 288–297, Mar. 2013, doi: 10.1049/iet-gtd.2012.0288.

[24] W. D. Oliveira, J. P. A. Vieira, U. H. Bezerra, D. A. Martins, and B. D. G. Rodrigues, "Power system security assessment for multiple contingencies using multiway decision tree," *Electr. Power Syst. Res.*, vol. 148, pp. 264–272, Jul. 2017, doi: 10.1016/j.epsr.2017.03.029.

[25] X. Li, T. Jiang, G. Liu, L. Bai, H. Cui, and F. Li, "Bootstrap-based confidence interval estimation for thermal security region of bulk power grid," *Int. J. Elect. Power Energy Syst.*, vol. 115, Feb. 2020, Art. no. 105498, doi: 10.1016/j.ijepes.2019.105498.

[26] Y. Zeng and Y. Yu, "A practical direct method for determining dynamic security regions of electrical power systems," in *Proc. Int. Conf. Power Syst. Technol.*, Kunming, China, vol. 2, Oct. 2002, pp. 1270–1274, doi: 10.1109/ICPST.2002.1047606.

[27] A. Xue, F. F. Wu, Q. Lu, and S. Mei, "Power system dynamic security region and its approximations," *IEEE Trans. Circuits Syst. I, Reg. Papers*, vol. 53, no. 12, pp. 2849–2859, Dec. 2006, doi: 10.1109/TCSI.2006.883860.

[28] M. Pourbehzadi, T. Niknam, J. Aghaei, G. Mokryani, M. Shafie-khah, and J. P. S. Catalão, "Optimal operation of hybrid AC/DC microgrids under uncertainty of renewable energy resources: A comprehensive review," *Int. J. Electr. Power Energy Syst.*, vol. 109, pp. 139–159, Jul. 2019, doi: 10.1016/j.ijepes.2019.01.025.

[29] S. A. M. Javadian, M.-R. Haghifam, S. M. T. Bathaee, and M. F. Firoozabad, "Analysis of protection system's risk in distribution networks with DG," *Int. J Electr. Power Energy Syst.*, vol. 44, no. 1, pp. 688–695, Jan. 2013, doi: 10.1016/j.ijepes.2012.08.034.

[30] V. G. Phillipe and J. T. Saraiva, "State-of-the-art of transmission expansion planning: A survey from restructuring to renewable and distributed electricity markets," *Int. J. Elect. Power Energy Syst.*, vol. 111, pp. 411–424, Oct. 2019, doi: 10.1016/j.ijepes.2019.04.035.

[31] Y. X. Yu and W. P. Luan, "Practical dynamic security region of power system," *Proc. CSEE*, vol. 13, no. 3, pp. 14–22, Nov. 1990.

[32] Y. X. Yu and J. K. Lin, "Practical analytic expression of power system dynamic security region's boundary," *J. Tianjin Univ.*, vol. 30, no. 1, pp. 1–8, 1997.

[33] Y. Zeng, J. C. Fan, F. Lu, Y. G. Fang, and Y. X. Yu, "Practical dynamic security regions of bulk power system," *Automat. Electr. Power Syst.*, vol. 25, no. 16, pp. 6–10, 2001.

[34] L. Min, Y. X. Yu, S. T. Lee, and Z. Pei, "Identification method of instability modes and its application in dynamic security region," *Automat. Electr. Power Syst.*, vol. 28, no. 11, pp. 28–32, 2004, doi: 1000-1026(2004)28:11<28:SWMTSB>2.0.TX.2-I.

[35] Z. F. Feng, Y. X. Yu, and Y. Zeng, "An intercept method for determining practical dynamic security regions of power systems," *Automat. Electr. Power Syst.*, vol. 30, no. 6, pp. 18–22, 2006, doi: 1000-3673(2006)30:6<18:QDDLXT>2.0.TX;2-T.

[36] Y. Zeng, Y. X. Yu, and H. J. Jia, "Computing practical dynamic security region by technology of power sensitivity analysis," *J. Tianjin Univ.*, vol. 39, no. 1, pp. 76–82, 2006.

[37] C. Qin, Y. L. Liu, and Y. X. Yu, "Dynamic security region of power systems with double fed induction generator," *Trans. China Electro. Tech. Soc.*, vol. 30, no. 18, pp. 157–163, 2015, doi: 1000-6753(2015)30:18<157:HSKFJD>2.0.TX;2-K.

[38] K. F. Hou, Y. X. Yu, S. T. Lee, and Z. Pei, "Reduction and reconstruction of power system practical dynamic security region," *Automat. Electr. Power Syst.*, vol. 28, no. 23, pp. 16–21, Dec., 2004, doi: 1000-1026(2004)28:23<16:DLXTSY>2.0.TX.2-L.

[39] W. Liu, P. Li, W. Yang, and C. Y. Chung, "Optimal energy flow for integrated energy systems considering gas transients," *IEEE Trans. Power Syst.*, vol. 34, no. 6, pp. 5076–5079, Nov. 2019, doi: 10.1109/TPWRS.2019.2929685.

[40] X. Liu, J. Wu, N. Jenkins, and A. Bagdanavicius, "Combined analysis of electricity and heat networks," *Appl. Energy*, vol. 162, pp. 1238–1250, Jan. 2016, doi: 10.1016/j.apenergy.2015.01.102.

[41] A. Shabanpour-Haghighi and A. R. Seifi, "An integrated steady-state operation assessment of electrical, natural gas, and district heating networks," *IEEE Trans. Power Syst.*, vol. 31, no. 5, pp. 3636–3647, Sep. 2016, doi: 10.1109/TPWRS.2015.2486819.

[42] J. Yu, L. Guo, M. Ma, S. Kamel, W. Li, and X. Song, "Risk assessment of integrated electrical, natural gas and district heating systems considering solar thermal CHP plants and electric boilers," *Int. J. Electr. Power Energy Syst.*, vol. 103, pp. 277–287, Dec. 2018, doi: 10.1016/j.ijepes.2018.06.009.

[43] R. Storn and K. Price, "Differential evolution a simple and efficient adaptive scheme for global optimization over continuous spaces," *J. Global Optim.*, vol. 11, no. 4, pp. 341–359, Mar. 1997.

[44] A. G. Babu, J. Jerald, A. N. Haq, V. M. Luxmi, and T. P. Vigneswaralu, "Scheduling of machines and automated guided vehicles in FMS using differential evolution," *Int. J. Prod. Res.*, vol. 48, no. 16, pp. 4683–4699, Aug. 2010, doi: 10.1080/00207540903049407.

[45] V. V. D. Melo and G. L. C. Carosio, "Investigating multi-view differential evolution for solving constrained engineering design problems," *Expert Syst. Appl.*, vol. 40, no. 9, pp. 3370–3377, Jul. 2013, doi: 10.1016/j.eswa.2012.12.045.

[46] M. M. Ali and W. X. Zhu, "A penalty function-based differential evolution algorithm for constrained global optimization," *Comput. Optim. Appl.*, vol. 54, no. 3, pp. 707–739, Apr. 2013, doi: 10.1007/s10589-012-9498-3.

[47] J.-G. Juang and S.-T. Yu, "Disturbance encountered landing system design based on sliding mode control with evolutionary computation and cerebellar model articulation controller," *Appl. Math. Model.*, vol. 39, no. 19, pp. 5862–5881, Oct. 2015, doi: 10.1016/j.apm.2015.04.005.

[48] Z. Yang, Q. Yu, W. Dong, X. Gu, W. Qiao, and X. Liang, "Structure control classification and optimization model of hollow carbon nanosphere core polymer particle based on improved differential evolution support vector machine," *Appl. Math. Model.*, vol. 37, nos. 12–13, pp. 7442–7451, Jul. 2013, doi: 10.1016/j.apm.2013.02.037.

[49] J. A. K. Suykens, T. Van Gestel, J. D. Brabanter, and B. D. Moor, *Least Square Support Vector Machines*. Singapore: World Scientific, 2002.

SANIYE MAIHEMUTI received the B.Eng. and M.Eng. degrees in electrical engineering from Xinjiang University, Xinjiang, China, in 2016 and 2018, respectively, where she is currently pursuing the Ph.D. degree in power system stability and control with the School of Electrical Engineering. Her research interests include power system stability, control, and integration of the renewable resources.

WEIQING WANG received the B.Eng. degree in electrical engineering from Xinjiang University, in 1983, and the M.Eng. degree in electrical engineering from the Department of Electrical Engineering, Zhejiang University, in 1990. He is currently the Dean of the Department of Electrical Engineering, Xinjiang University. His research interests include the key components of large wind turbine, the detection technology of wind turbines, power system security, and stability and its control and protection, as well as the micro power grid control and fault diagnosis.

HAIYUN WANG received the B.Eng. degree in electrical engineering from Xinjiang University, Xinjiang, China, in 1995, and the M.Eng. degree in electrical engineering from the Dalian University of Technology, Dalian, China, in 1996. She is currently a Professor with the Department of Electrical Engineering, Xinjiang University, and the Deputy Secretary of the new energy industry innovation alliance. Her research interests include the key components of large wind turbine, the detection technology of wind turbines, as well as power system security and stability and its control and protection.

JIAHUI WU received the B.Eng. degree in control engineering from the Beijing University of Chemical Technology, Beijing, China, in 2011, and the M.Eng. and the Ph.D. degrees in electrical engineering from Xinjiang University, Xinjiang, China, in 2015 and 2018, respectively. She is currently an Associate Professor with the Department of Electrical Engineering, Xinjiang University. Her research interests include power system stability and integration of the renewable resources.

XUAN ZHANG received the B.E. and M.E. degrees in electrical engineering from Xinjiang University, China, in 2016 and 2019, respectively. He currently works with China Ship Building (Handan) Perry Special Gas Company Ltd. His research interests include power system stability and control and integration of the renewable resources.